AD-A012 875

FLOW-FIELD MEASUREMENTS IN THE WINDWARD SURFACE SHOCK LAYER OF SPACE SHUTTLE ORBITER CONFIGURATIONS AT MACH NUMBER 8

W. R. Martindale, et al

Arnold Engineering Development Center

Prepared for:

ARO, Incorporated
National Aeronautics and Space Administration

July 1975

AEDC-TR-75-5

219084

FLOW-FIELD MEASUREMENTS IN THE WINDWARD SURFACE SHOCK LAYER OF SPACE SHUTTLE ORBITER CONFIGURATIONS AT MACH NUMBER 8

VON KÁRMÁN GAS DYNAMICS FACILITY
ARNOLD ENGINEERING DEVELOPMENT CENTER
AIR FORCE SYSTEMS COMMAND
ARNOLD AIR FORCE STATION, TENNESSEE 37389

July 1975

Final Report for Period September 29, 1973 — May 9, 1974

Approved for public release; distribution unlimited.

Prepared for

NATIONAL AERONAUTICS AND SPACE ADMINISTRATION (JSC)
HOUSTON, TEXAS 77058

NOTICES

When U. S. Government drawings specifications, or other data are used for any purpose other than a definitely related Government procurement operation, the Government thereby incurs no responsibility nor any obligation whatsoever, and the fact that the Government may have formulated, furnished, or in any way supplied the said drawings, specifications, or other data, is not to be regarded by implication or otherwise, or in any manner licensing the holder or any other person or corporation, or conveying any rights or permission to manufacture, use, or sell any patented invention that may in any way be related thereto.

Qualified users may obtain copies of this report from the Defense Documentation Center.

References to named commercial products in this report are not to be considered in any sense as an endorsement of the product by the United States Air Force or the Government.

This report has been reviewed by the Information Office (OI) and is releasable to the National Technical Information Service (NTIS). At NTIS, it will be available to the general public, including foreign nations.

APPROVAL STATEMENT

This technical report has been reviewed and is approved for publication.

FOR THE COMMANDER

JIMMY W. MULLINS
Lt Colonel, USAF
Chief Air Force Test Director, VKF
Directorate of Test
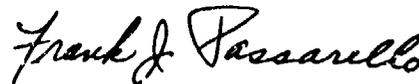
FRANK J. PASSARELLO
Colonel, USAF
Director of Test

REPORT DOCUMENTATION PAGE		READ INSTRUCTIONS BEFORE COMPLETING FORM
1. REPORT NUMBER AEDC-TR-75-5	2. GOVT ACCESSION NO.	3. RECIPIENT'S CATALOG NUMBER
4. TITLE (and Subtitle) FLOW-FIELD MEASUREMENTS IN THE WINDWARD SURFACE SHOCK LAYER OF SPACE SHUTTLE ORBITER CONFIGURATIONS AT MACH NUMBER 8		5. TYPE OF REPORT & PERIOD COVERED Final Report–September 29, 1973 – May 9, 1974
		6. PERFORMING ORG. REPORT NUMBER
7. AUTHOR(s) W. R. Martindale and L. D. Carter, ARO, Inc.		8. CONTRACT OR GRANT NUMBER(s)
9. PERFORMING ORGANIZATION NAME AND ADDRESS Arnold Engineering Development Center (XO) Arnold Air Force Station, Tennessee 37389		10. PROGRAM ELEMENT, PROJECT, TASK AREA & WORK UNIT NUMBERS Program Element 921E Project 9705
11. CONTROLLING OFFICE NAME AND ADDRESS National Aeronautics and Space Administration (JSC/ES3) Houston, Texas 77058		12. REPORT DATE July 1975
		13. NUMBER OF PAGES 53
14. MONITORING AGENCY NAME & ADDRESS(if different from Controlling Office)		15. SECURITY CLASS. (of this report) UNCLASSIFIED
		15a. DECLASSIFICATION DOWNGRADING SCHEDULE N/A

16. DISTRIBUTION STATEMENT (of this Report)

Approved for public release; distribution unlimited.

17. DISTRIBUTION STATEMENT (of the abstract entered in Block 20, if different from Report)

18. SUPPLEMENTARY NOTES

Available in DDC

19. KEY WORDS (Continue on reverse side if necessary and identify by block number)

flow fields	shock (mechanics)
measurements	Space Shuttle Orbiter
surfaces (windward)	shape
layers	Mach number

20. ABSTRACT (Continue on reverse side if necessary and identify by block number)

Pitot pressure and total-temperature measurements were made in the windward surface shock layer of two 0.0175-scale space shuttle orbiter models at simulated re-entry conditions. Corresponding surface static pressure measurements were also made. Flow properties at the edge of the model boundary layer were derived from these measurements and compared with values calculated using conventional methods. Measurements were made at Mach

DD FORM 1473   EDITION OF 1 NOV 65 IS OBSOLETE

20. ABSTRACT (Continued)

number 8, angles of attack from 15 to 35 deg, and Reynolds
numbers, based on model length, of 1.3×10^6 and 2.1×10^6.

PREFACE

1

CONTENTS

ILLUSTRATIONS

3

TABLES

APPENDIX

1.0 INTRODUCTION

An understanding of the flow-field structure of a re-entry vehicle, such as the Space Shuttle Orbiter is essential if hypersonic wind tunnel data (particularly convective heating data) are to be reliably extrapolated to flight conditions. Specific areas of interest in the vehicle flow field are shock wave standoff distance, distribution of flow-field properties in the inviscid shock layer, flow properties at the edge of the boundary layer, and details of the boundary-layer flow. The definition of flow properties at the edge of the laminar boundary layer is of particular importance because most boundary-layer transition correlations (see Ref. 1 for example) use these properties.

The primary objective of the present tests was the determination of flow properties at the edge of laminar boundary layers on current Space Shuttle Orbiter configurations. Pitot pressure, total-temperature, and surface static pressure measurements were used with the isentropic flow relations to derive these properties. Secondary objectives included obtaining inviscid shock layer flow-field property distributions, shock wave standoff measurements, and boundary-layer flow details.

The tests were conducted in the Hypersonic Wind Tunnel (B) of the von Kármán Gas Dynamics Facility (VKF), at Mach number 8 using specially constructed pitot pressure and total-temperature probes. The tests were conducted in two phases, designated OH9 and OH52, each using a 0.0175-scale model of the then current Space Shuttle Orbiter configuration. Model angle of attack was varied from 15 to 35 degrees and Reynolds numbers, based on model reference length, were 1.3×10^6 and 2.1×10^6.

A complementary analytical study was undertaken to develop techniques to extrapolate the present boundary-layer-edge measurements to flight conditions. This study is documented in Ref. 2.

2.0 APPARATUS

2.1 WIND TUNNEL

Tunnel B is a continuous, closed-circuit, 50-in.-diam hypersonic tunnel having Mach 6 and 8 axisymmetric contoured nozzles. With the Mach 8 nozzle, this tunnel can be operated over the stagnation pressure

range of 50 to 850 psia at a maximum stagnation temperature of 1350°R. The tunnel is equipped with a model injection system with which the model may be injected and retracted without interrupting the flow. A description of the tunnel may be found in Ref. 3.

2.2 MODELS

2.2.1 OH9—Phase

The model used during the OH9 phase of testing was supplied by Rockwell International and was a 0.0175-scale model of the Space Shuttle Orbiter Configuration 139. It was designated as Model 29-0 and is defined on Rockwell Drawing VL70-000139. This model was constructed of 15-5 stainless steel and had no movable control surfaces. The basic configuration is shown in Fig. 1, and a photograph of the model is presented in Fig. 2. Twenty-one static pressure orifices located on the lower surface of the model were made of 0.063-in.-OD stainless steel tubing which provided orifice diameters of 0.040 in. Also located on the lower surface were three 1/8-in. Chromel®-constantan surface thermocouple gages which were used to record the model surface temperature. The locations of the static pressure orifices and surface thermocouples are shown in Fig. 3 and listed in Table 1.

2.2.2 OH52—Phase

The OH52 phase model was a revised version of the OH9 model and was designated as 29-0-Modified. This model is defined on Rockwell Drawing VL70-000140B. It was constructed of 15-5 stainless steel and had no movable control surfaces. The principal configuration changes from the 139 configuration were in nose shape and wing incidence angle. A comparison of lower surface contours for the two models is shown in Fig. 4. The twenty-six pressure orifice and ten thermocouple gage locations on the lower surface of this model are shown in Fig. 3 and listed in Table 2.

2.3 INSTRUMENTATION AND MEASUREMENT PRECISION

2.3.1 Tunnel Instrumentation

The Tunnel B stilling chamber pressure was measured with a 1000-psid transducer referenced to a near vacuum. The estimated uncertainty

8

of ± 0.2 percent of the calibrated range for this transducer is based on periodic comparison with a secondary standard. The stilling chamber temperature was measured with Chromel®-Alumel® thermocouples which have an uncertainty of ± 0.5 percent. The free-stream Mach number uncertainty is ± 0.30 percent of the calibrated Mach number for the Mach 8 nozzle. The uncertainties of the free-stream properties were estimated by means of the Taylor series method of error propagation.

Uncertainties, $\pm$ Percent

M_∞	p_0	T_0	p_∞	T_∞	p_0'	q_∞	Re/ft
0.3	0.8	0.5	2.1	0.8	1.5	1.5	1.4

2.3.2 Model Surface Data

The model surface pressures were measured with 1-psid transducers with an uncertainty of ± 1 percent. Using the Taylor series method of error propagation with this and the p_0' uncertainty, the uncertainty of p_m/p_0' is 1.8 percent.

The model surface temperatures were measured with Chromel-constantan coaxial surface thermocouple gages. Precision of the thermocouple measurements is estimated to be $\pm 3°R$ considering wire and instrument uncertainties.

2.3.3 Flow-Field Survey Systems

The flow-field surveys were performed with a 4-degree-of-freedom remote drive mechanism. This system positioned the probes over the stations to be surveyed and pitched the survey drive axis, Zp, such that the survey would be made as nearly normal to the model centerline as possible. The probe pitch drive was limited to 29 deg; therefore, surveys made for model angles of attack of 30 and 35 deg were slightly off the normal. The survey stations were located within 0.1 inch of the surface pressure orifice used to reduce the data, and the precision of the probe translation was estimated to be ± 0.003 inches.

The pitot pressure probes were connected to 15-psid transducers which were calibrated for a 5-psid range. For this range, these transducers have an uncertainty of ± 0.01 psia.

2.3 4 OH9—Phase Probes

Because of limited vertical drive, two different length probe supports (Fig. 5) were required to cover the ten model survey stations during the OH9 phase of testing. Each of these flow-field survey probe supports had two Chromel-Alumel, unshielded, total-temperature probes positioned outboard of the lower of two pitot probes. Temperature probe TT_2 was 0.010 in. in diameter and was used as the primary instrument. Probe TT_1 was 0.020 in. in diameter and was considered as a backup for TT_2. Probes similar to TT_1 and TT_2, previously tested in Tunnel B, exhibited a free-stream recovery factor, TT/T_o, of about 0.9.

The lower pitot probe, pp_1, was constructed of 0.020-in.-OD tubing tapered to 0.014 in. at the tip and had an inside diameter of 0.010 in. This small tubing was used to minimize the flow disturbances and improve the data resolution in the model boundary layer. The other pitot probe, pp_2, was located about 1.0 in. above pp_1 and was constructed of 0.093-in.-OD tubing.

2.3.5 OH52—Phase Probes

A single probe support was used during the OH52 phase of testing (Fig. 6). The temperature probe, TT_1, and the lower pitot probe, pp_1, were similar to the corresponding probes of the OH9 phase. Probe pp_2 was located 0.584 in. above pp_1 and constructed of 0.093-in.-OD tubing, flattened at the tip to a height of 0.052 in.

The uncertainty of the boundary-layer thicknesses derived from the total-temperature profiles is estimated to have been ±0.006 in. based on data repeatability and smoothness. Similarly, the boundary-layer-edge Mach number uncertainty is estimated to be ±0.07.

3.0 PROCEDURE

3.1 TEST PROCEDURE

When investigating the flow field of a configuration such as the Shuttle Orbiter which may have velocity gradients at the boundary-layer edge, the boundary-layer thickness can best be determined from the total-temperature profiles. The existence of velocity gradients in the inviscid shock layer does not alter the adiabatic nature of the flow,

hence, the total temperature remains constant through the flow field until the boundary layer is reached. When the effect of viscous dissipation becomes significant, i.e., when the boundary layer is entered, the total temperature decreases. At the model surface the total temperature is, of course, equal to the model temperature. The magnitude of the total-temperature inflection at the boundary-layer edge is enhanced by lowering the model wall temperature, so during the tests several measures were used to minimize model wall temperature.

To obtain minimum wall temperature flow-field surveys, the initial model surface temperature and the time of aerodynamic heating of the model were controlled. The model, therefore, was retracted from the tunnel flow between surveys and cooled to about 530°R with air jets. During this time, the probes were positioned in the test section to a predetermined location for the next survey. The model was then injected into the tunnel and the survey was initiated by driving the probes toward the model surface. When the lower pitot probe approached the vicinity of the model boundary layer where a high pitot pressure gradient was encountered, the data were recorded in a drive-pause manner to accommodate the longer pressure stabilization time in this region. When the lower pitot probe made contact with the model surface an electrical foul circuit was triggered, recording the final survey data point and establishing the probe height zero. An additional data point was taken after the pitot pressure had completely stabilized. After driving the probes clear, the model was retracted from the tunnel for cooling and the cycle repeated for the next run.

The model surface pressure data were obtained independently of the flow-field survey data.

3.2 TEST CONDITIONS

The tests were conducted at a nominal free-stream Mach number of 8 at a tunnel stilling chamber temperature of 1340°R. The other test conditions were as follows:

Nominal Test Conditions

M_∞	p_o, psia	p_∞, psia	T_∞, °R	q_∞, psia	Re/ft $\times 10^{-6}$
7.92	150	0.016	99	0.72	0.7
7.95	250	0.027	98	1.18	1.1

Test summaries are given in Table 3.

3.3 DATA REDUCTION

The survey heights for the probes were computed using the geometric center of each probe and the relative position of the probes. The zero probe height point, obtained when the lower pitot probe (pp_1) made electrical contact with the model, was used to reference all probe heights to the model surface.

Since the total-temperature probes were unshielded, there was a radiation loss associated with each measurement. In the inviscid shock layer this loss was about 5 percent. Since it did not affect the definition of the boundary-layer edge, no radiation loss corrections were applied to the data. However, if comparisons are made with calculations or quantities are derived using these total-temperature measurements, a correction should be applied. The simplest correction is to select a point exterior to the boundary layer and obtain a correction factor by setting TT/T_O equal to 1.0 at this point. The rest of the readings would then be multiplied by the correction factor.

In spite of the efforts to reduce pitot pressure stabilization error as mentioned previously, significant errors were suspected, particularly in the interior of the boundary layer. To quantify error estimates, calculations were made using a pressure stabilization computer program. The results indicated an error increasing from about 2.5 percent at the boundary-layer edge to about 30 percent at the model surface. A graphical presentation of this result will be discussed in a subsequent section.

The boundary-layer thickness, δ, was determined from the total-temperature profile by selecting the point at which the measured value was 0.995 of the maximum measured value. The measured pitot pressure at this point and the corresponding model surface pressure were then used to determine the boundary-layer-edge Mach number. The other edge conditions were computed using the Mach number and the isentropic flow relations given in Appendix A. The computed edge conditions are summarized in Tables 4 and 5.

Note that the present boundary-layer-edge conditions depend on the value of total-temperature ratio used in the definition. For example, values of 0.99 or 0.999 times the maximum measured total temperature could have been used to define δ. However, the edge values obtained are consistent and are comparable to numerical results such as those of Ref. 2 where the boundary-layer edge was similarly defined.

4.0 RESULTS AND DISCUSSION

4.1 STATIC PRESSURE

Model centerline static pressure measurements from the 139 and 140B configurations are compared in Fig. 7. The two sets of measurements are in good agreement for X/L values less than or equal to 0.8 and diverge at larger values. These results are consistent with the local body surface contours shown in Fig. 4.

Also shown in Fig. 7 are modified Newtonian and tangent cone calculations for the 139 configuration. The data generally fall between the two sets of calculated values which is consistent with data from similar configurations (see Ref. 4 for example).

Spanwise static pressure measurements from the 139 configuration at an X/L value of 0.8 and 30-deg angle of attack are compared with calculations using three methods in Fig. 8. The measurements rise from agreement with the tangent cone value near the centerline to agreement with tangent wedge values at the most outboard measurement station.

A summary of wing static pressure measurements is shown in Fig. 9 along with calculated values for 2Y/B = 0.6. Calculated values for the other spanwise stations are not significantly different and are not shown. Once again, the trend of increasing pressure with spanwise distance can be seen.

4.2 PITOT PRESSURE AND TOTAL-TEMPERATURE PROFILES

A typical pitot pressure profile from the 139 configuration is shown in Fig. 10. The bow shock is located about one inch from the model surface. The pitot pressure profile is smooth from the shock to the model surface with no evidence of the boundary-layer-edge location.

The total-temperature profile corresponding to the pitot pressure profile of Fig. 10 is shown in Fig. 11. In contrast to the pitot pressure profile, the vicinity of the boundary-layer edge can be easily seen as the area where the total temperature rapidly decreases. The theoretical aspects of using total-temperature or total enthalpy profiles to define boundary-layer-edge conditions are discussed in Ref. 2. The present

13

definition of the boundary-layer edge (δ) is the point where $TT/TT_{max} = 0.995$ as discussed in Section 3.3.

In the present tests, the pitot probe diameter was not necessarily neglible with respect to boundary-layer thickness, hence, probe interference with the boundary layer might be suspected. Monaghan (Ref. 5) discusses three types of profile distortions that may occur if the pitot probe is too large. They are as follows:

(1) A peak in the profile at the outer edge of the boundary layer,

(2) A displacement of the main body of the profile, and

(3) A distortion of the profile near the wall.

The most important potential effect with respect to present data was the profile peak at the edge of the boundary layer since boundary-layer-edge properties were the primary objective. Galezowski (Ref. 6) studied the effect of circular pitot probe diameter on boundary-layer profiles and found that if the probe diameter-to-boundary-layer thickness ratio was less than 0.29, no profile peak (or distortion) occurred at the boundary-layer edge.

An enlargement of the pitot pressure ratio profile for the region near the model surface from Fig. 10 is shown in Fig. 12. In this case the probe diameter-to-boundary-layer thickness ratio was 0.21 which, according to Galezowski criterion, should be adequate to avoid profile peaking at the boundary-layer edge. Examination of Fig. 12 indicates that this is indeed the case. In three centerline surveys the probe diameter-to-boundary-layer thickness did exceed 0.29 by a small amount, but no profile peaking was noted.

The profile displacement effect noted above results from the effective center of pressure being shifted from the geometric center of the probe. Reference 5 states that this effect is probably quite small in supersonic boundary layers.

Profile distortion near a model surface is probably related to a local three-dimensional separation in the vicinity of the probe tip as discussed in Ref. 7. In Ref. 7 it was suggested that profile data, at points where the probe wall separation distance is on the order of the probe diameter, should probably be disregarded. The region of possible probe wall interference is shown in Fig. 12.

Also shown in Fig. 12 is the estimate of the true pitot pressure profile based on pressure stabilization calculations as discussed in Section 3.3. The validity of this estimate is confirmed since it agrees with the stabilized point with the probe on the model surface (see Section 3.1).

A comparison of centerline pitot pressure profiles for 139 and 140B configurations at an X/L value of 0.5 and 30-deg angle of attack is shown in Fig. 13. Differences are small as expected since body profile differences are small (Fig. 4).

Off-centerline pitot pressure profiles from the 140B configuration at values of 2Y/B of 0.4 and less were similar in nature to the centerline profiles. Profiles at 2Y/B greater than 0.4 were considerably different as can be seen from three examples in Fig. 14. These profiles are irregular, perhaps indicating the presence of shocks and expansions in the flow field.

The thinnest boundary-layer measurement recorded was 0.030 in. at a 2Y/B = 0.6 and X/L = 0.75. The probe diameter-to-boundary-layer thickness ratio in this case was 0.47, but only a small overshoot in pitot pressure at the edge of the boundary layer was noted.

4.3 BOUNDARY-LAYER THICKNESS

Centerline boundary-layer thickness measurements from the 139 configuration are shown in Fig. 15. A trend of decreasing thickness with increasing angle of attack can be seen. The rapid thickening of the boundary layer near the aft end of the vehicle is attributed to the combined effects of flow expansion (see Figs. 4 and 7) and three-dimensional flow convergence in this region. Centerline boundary-layer thicknesses from the 139 and 140B configurations are compared in Fig. 16. The 140B results indicated a slightly thicker boundary layer.

Spanwise distribution of boundary-layer thickness at an X/L of 0.8 for the 140B configuration is shown in Fig. 17. A rapid decrease in thickness is noted in the region between 2Y/B values of 0.4 to 0.6. This decrease may be related to a dramatic change in pitot pressure profiles between the two areas (compare Figs. 13 and 14). An oil-flow photograph of the 139 configuration from another test is shown in Fig. 18. Two streaks are noted in the region between 2Y/B values of 0.4 and 0.6. These streaks are in the area of the bow shock/wing interaction and apparently depict the transition from body-dominated flow to

that supported by the outer portion of the wing. Thus, the boundary-layer thinning in this area is attributed to the transition from body to outer-wing flow.

4.4 BOUNDARY-LAYER-EDGE MACH NUMBER

An illustration of a blunt body flow field typical of that found on the Space Shuttle lower surface is shown in Fig. 19. The parameter controlling local boundary-layer-edge conditions is the shock-wave angle at which the local streamline entering the boundary layer crossed the shock. The limiting values of shock crossing angle are then the normal shock present at the nose and the oblique shock angle perpendicular to the point under consideration.

A comparison of centerline boundary-layer-edge Mach number from the 139 configuration and calculated values based on the shock angle limits are shown in Fig. 20. The calculated values were obtained using isentropic flow relations with the measured static pressure and the total pressure downstream of a normal shock (denoted normal shock) or the total pressure downstream of an oblique shock whose angle was determined by tangent cone theory applied locally (denoted tangent cone). At all three angles of attack the boundary-layer-edge Mach numbers fall between the calculated limiting values, with a slight trend toward the tangent cone limit as angle of attack increases. This trend is expected since the nose flow, which is characterized by normal shock calculations, becomes less dominant as angle of attack increases.

Comparisons of boundary-layer-edge Mach numbers and thicknesses for the two Reynolds numbers at which data were obtained showed only minor differences and are not presented. A discussion of scaling the present data with respect to Reynolds number is given in Ref. 2.

A comparison of centerline boundary-layer-edge Mach numbers for the 139 and 140B configurations is shown in Fig. 21. There is close agreement except in the expansion region (X/L greater than 0.8).

Spanwise boundary-layer-edge Mach numbers from the 140B configuration at an X/L value of 0.8 are compared with calculated values in Fig. 22. The values rise with increasing spanwise distance until good agreement with tangent cone calculations is obtained at 2Y/B of 0.6. Again, this is expected since the outer portion of the wing is essentially free from nose bluntness effects.

A summary of boundary-layer-edge Mach numbers on the 140B wing is shown in Fig. 23 along with tangent wedge and tangent cone calculations for 2Y/B of 0.6. Except for the expansion region (XW/C > 0.6) the values are generally in good agreement with tangent cone calculations.

5.0 CONCLUSIONS

Pitot pressure and total-temperature profiles were measured in the windward surface shock layer of two 0.175-scale Space Shuttle Orbiter models. Surface static pressure measurements were also made. Boundary-layer-edge conditions were then derived from these measurements. Two distinctly different flow fields were found with the following characteristics:

Fuselage $(0 \leqslant 2Y/B < 0.4)$

1. Smooth pitot pressure profiles from the shock to the model surface and

2. Boundary-layer-edge Mach numbers that fall approximately midway between normal shock and tangent cone calculations.

Wing $(0.6 \leqslant 2Y/B < 1)$

1. Irregular pitot pressure profiles indicating a complex flow field and

2. Boundary-layer-edge Mach numbers that agree with tangent cone calculations.

REFERENCES

1. Helms, Vernon T. III. "Evaluation of Boundary-Layer-Transition Criteria for Space Shuttle Orbiter Entry." Paper No. 4 in NASA TM X-2507, Volume II, February 1972, pp. 683-704.

2. Adams, J. C., Jr., Martindale, W. R., Mayne, A. W. Jr., et al. "Real Gas Scale Effects on Hypersonic Laminar Boundary-Layer Parameters Including Effects of Entropy-Layer Swallowing." AEDC-TR-75-2, 1975.

3. Sivells, J. C. "Aerodynamic Design and Calibration of the VKF 50-Inch Hypersonic Wind Tunnels." AEDC-TDR-62-230 (AD299774), March 1963.

4. Matthews, R. K., Eaves, R. H., Jr., and Martindale, W. R. "Heat-Transfer and Flow-Field Tests of the McDonnell Douglas-Martin Marietta Space Shuttle Configurations." AEDC-TR-73-53 (AD759176), April 1973.

5. Monaghan, R. J. "The Use of Pitot Tubes in the Measurement of Laminar Boundary Layers in Supersonic Flow." AGARD Papers Presented at the Seventh Meeting of the Wind Tunnel and Model Testing Panel, AG19/P9, June 1955, Ottawa, Canada.

6. Galezowski, Stanley H. "Effects of Probe Tip Geometry and Size on Measurements in a Laminar Boundary Layer in Supersonic Flow." University of Toronto Institute of Aerophysics - TN-17, October 1957..

7. Morkovin, M. V. and Bradfield, N. S. "Probe Interference in Measurements in Supersonic Laminar Boundary Layers." Journal of the Aeronautical Sciences, Vol. 21, No. 11, November 1954, pp. 785-7.

8. Ames Research Staff. "Equations, Tables, and Charts for Compressible Flow." NACA-R-1135, 1953.
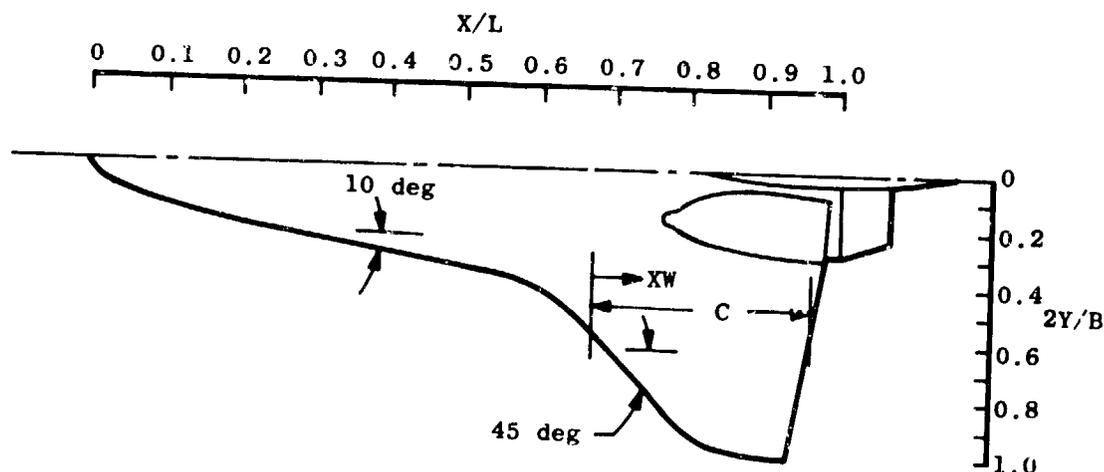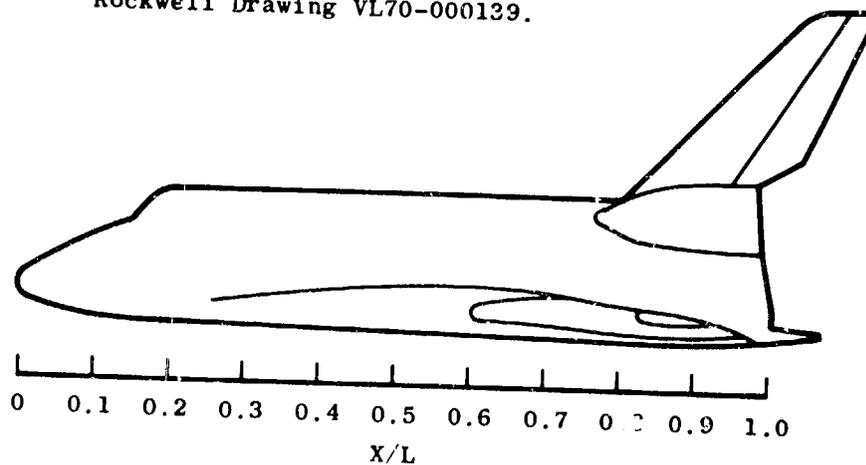
Figure 1. Rockwell International 139 Shuttle Orbiter configuration.

Figure 2. OH9 test installation photograph.
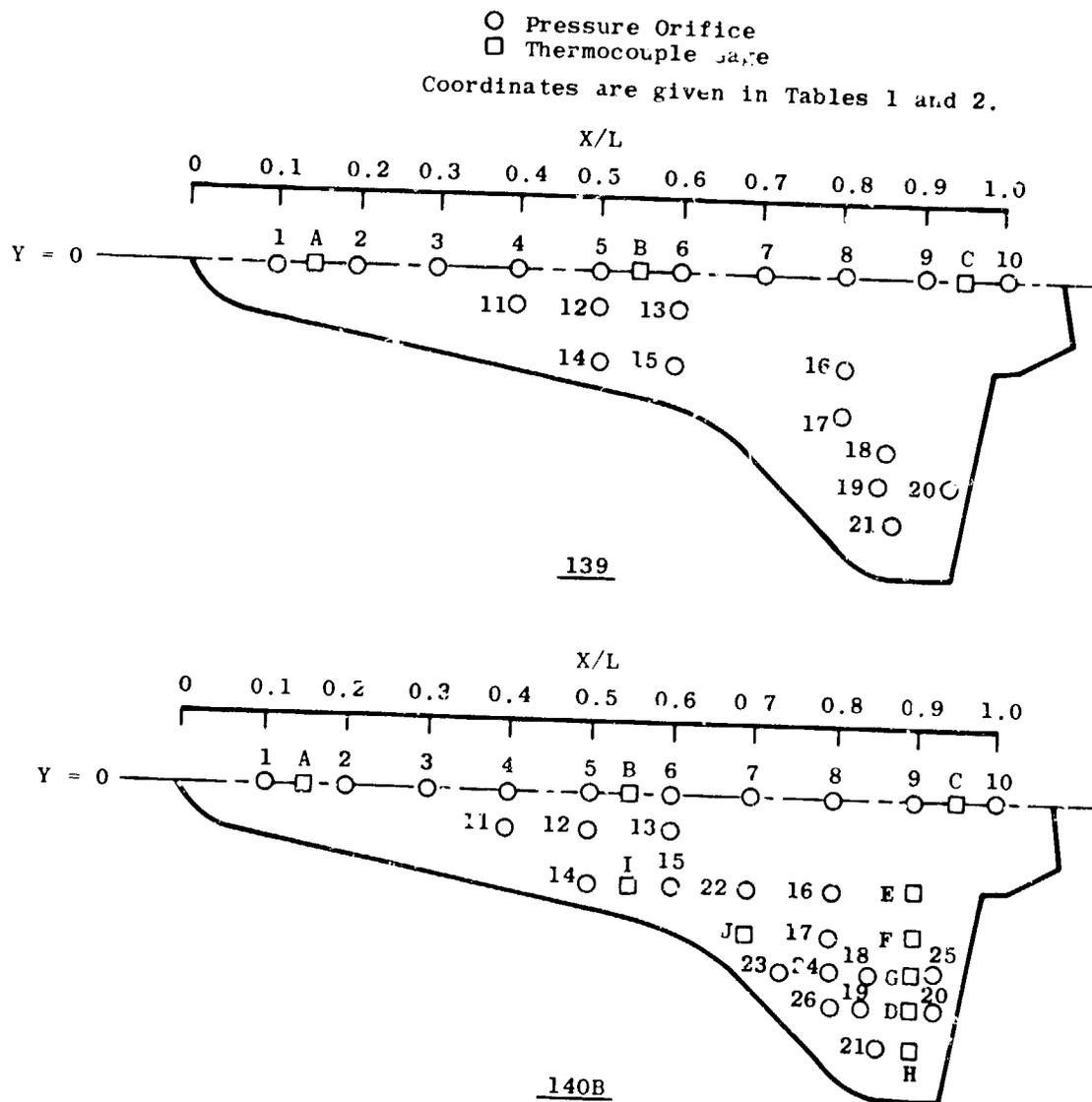
Figure 3. Pressure orifice and thermocouple gage locations.
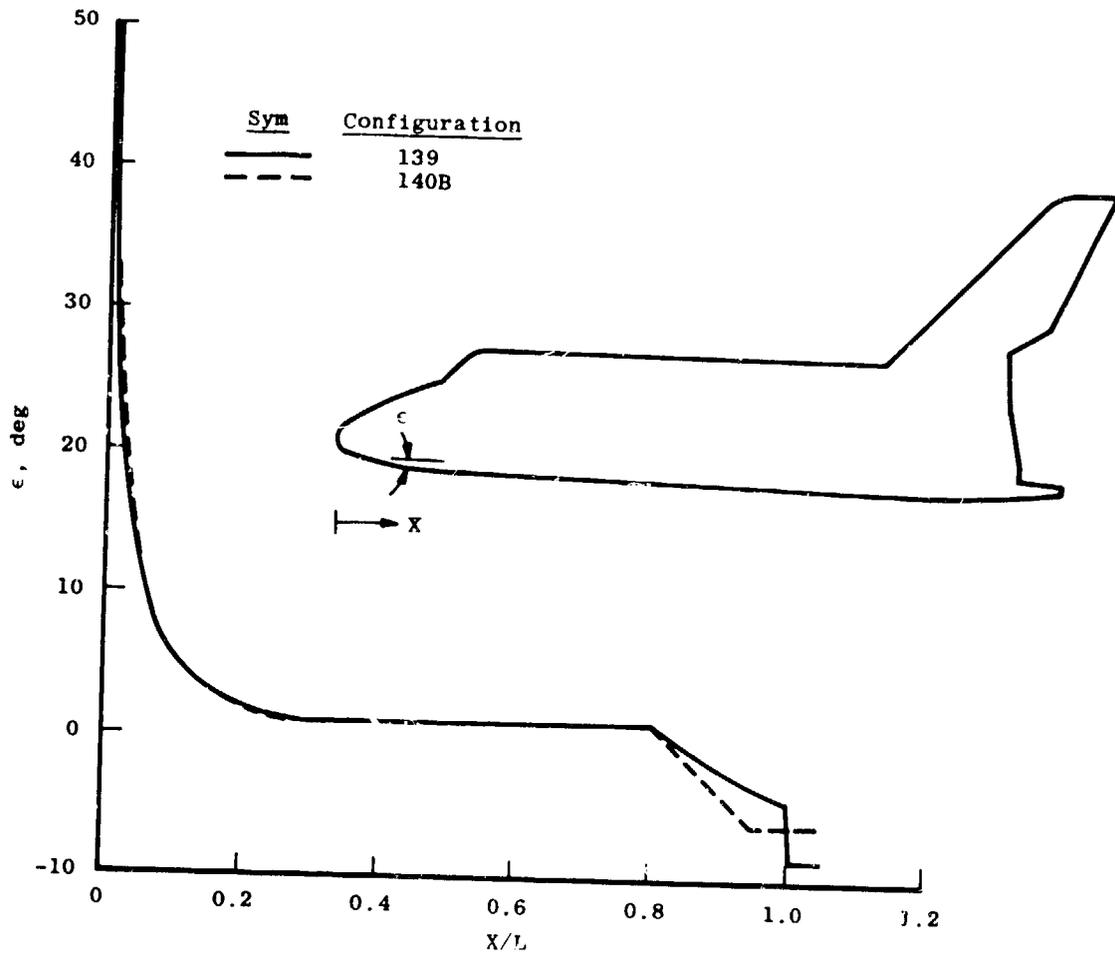
Figure 4. Windward surface centerline deflection angles of the 139 and 140B Space Shuttle Orbiters.
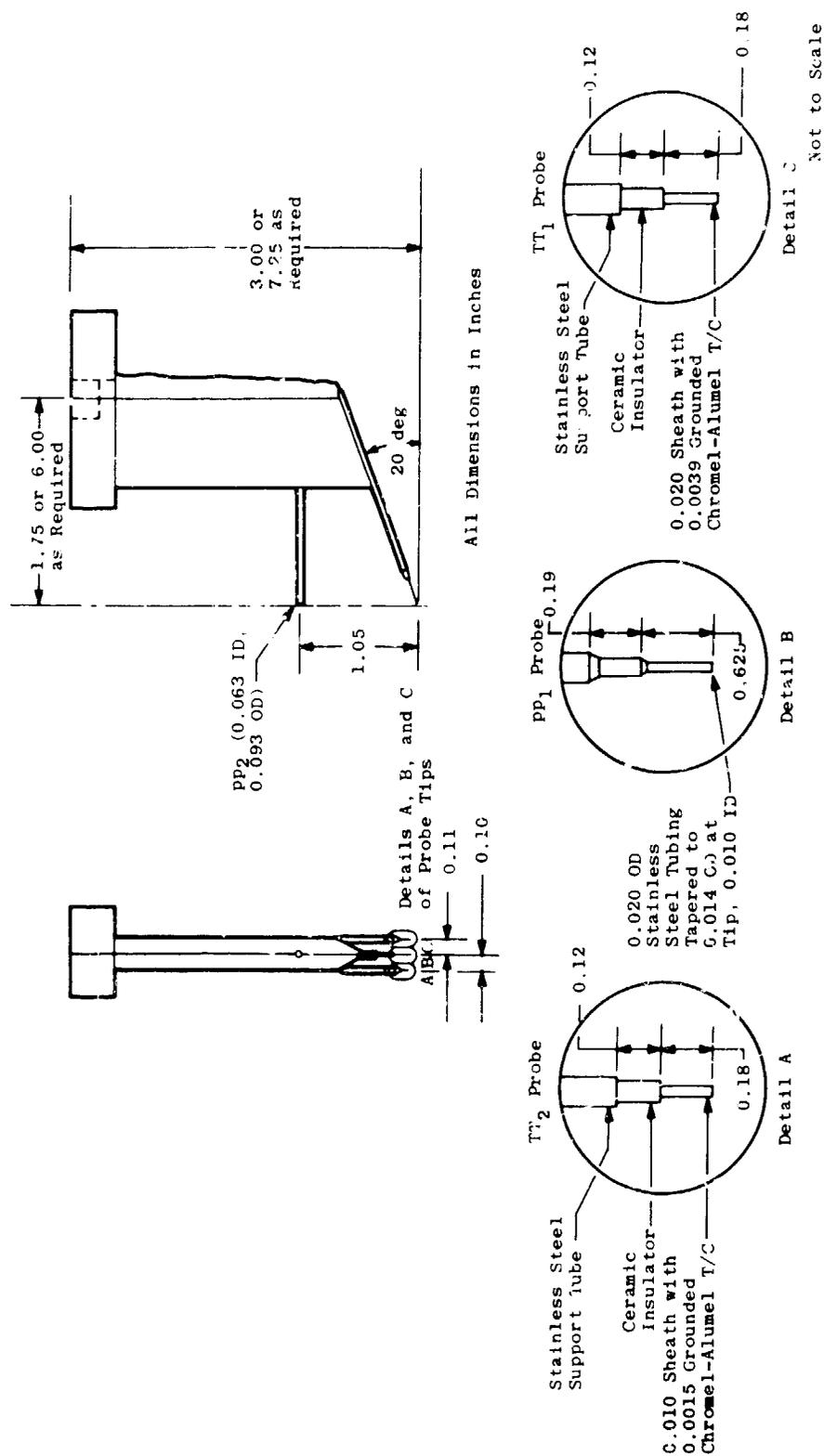
Figure 5. OH9 probe support.

All Dimensions in Inches

3.00 or 7.25 as required

1.75 or 6.00 as Required

20 deg

1.05

PP₂ (0.063 ID, 0.093 OD)

Details A, B, and C of Probe Tips

0.11

0.10

A|B|C

TT₁ Probe

Stainless Steel Support Tube

Ceramic Insulator

0.020 Sheath with 0.0039 Grounded Chromel-Alumel T/C

0.12

0.18

Detail C

Not to Scale

PP₁ Probe

0.19

0.625

0.020 OD Stainless Steel Tubing Tapered to 0.014 OD at Tip, 0.010 ID

Detail B

TT₂ Probe

Stainless Steel Support Tube

Ceramic Insulator

0.010 Sheath with 0.0015 Grounded Chromel-Alumel T/C

0.12

0.18

Detail A

pp$_2$ (0.020 x
0.085 Inside,
0.052 x 0.118
Outside)

6.00

7.25

0.584

20 deg

TT$_1$ Probe

pp$_1$ Probe

0.12

Stainless Steel
Support Tube

Stainless Steel
Support Tube

0.010 Sheath with
0.0015 Grounded
Chromel-Alumel T/C

0.18

0.140

Detail A

0.19

0.020 OD
Stainless
Steel Tubing
Tapered to
0.014 OD at
Tip, 0.010 ID

0.62

Detail B

All Dimensions in Inches

Figure 6. OH52 probe support.

24
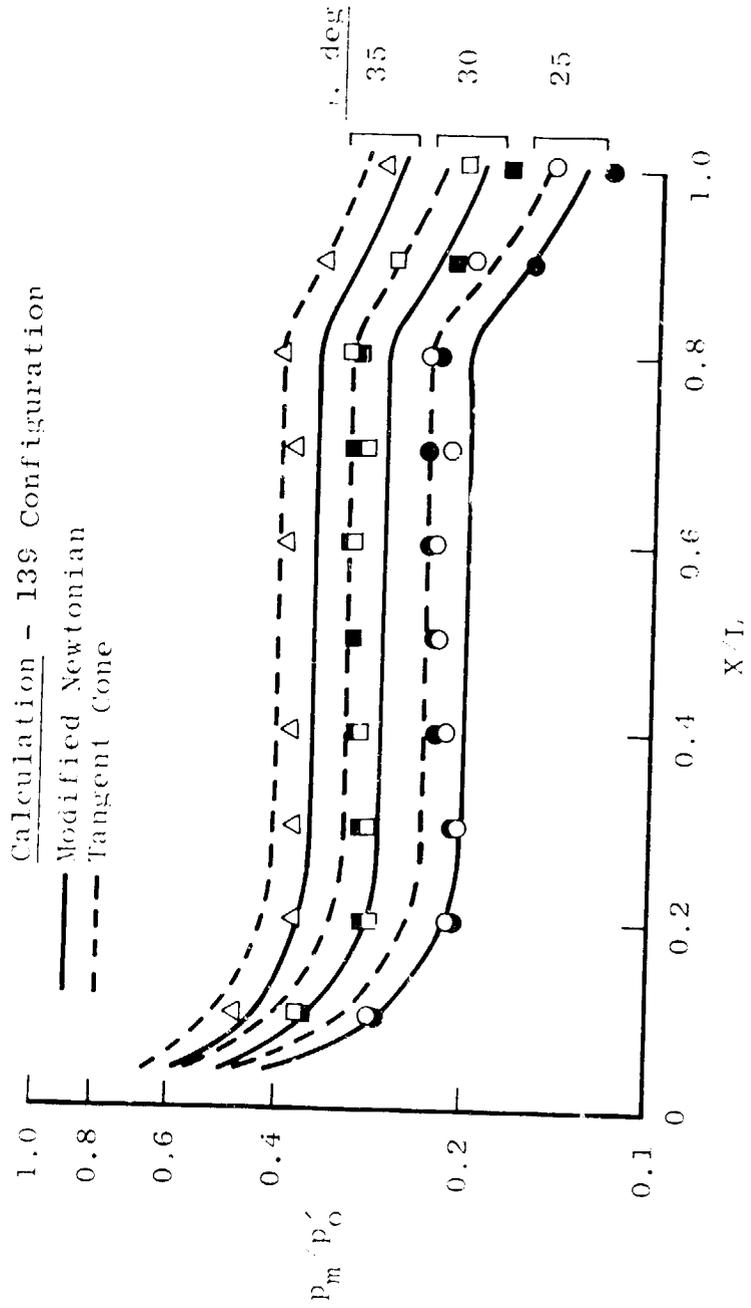
Figure 7. Centerline surface static pressure distributions.
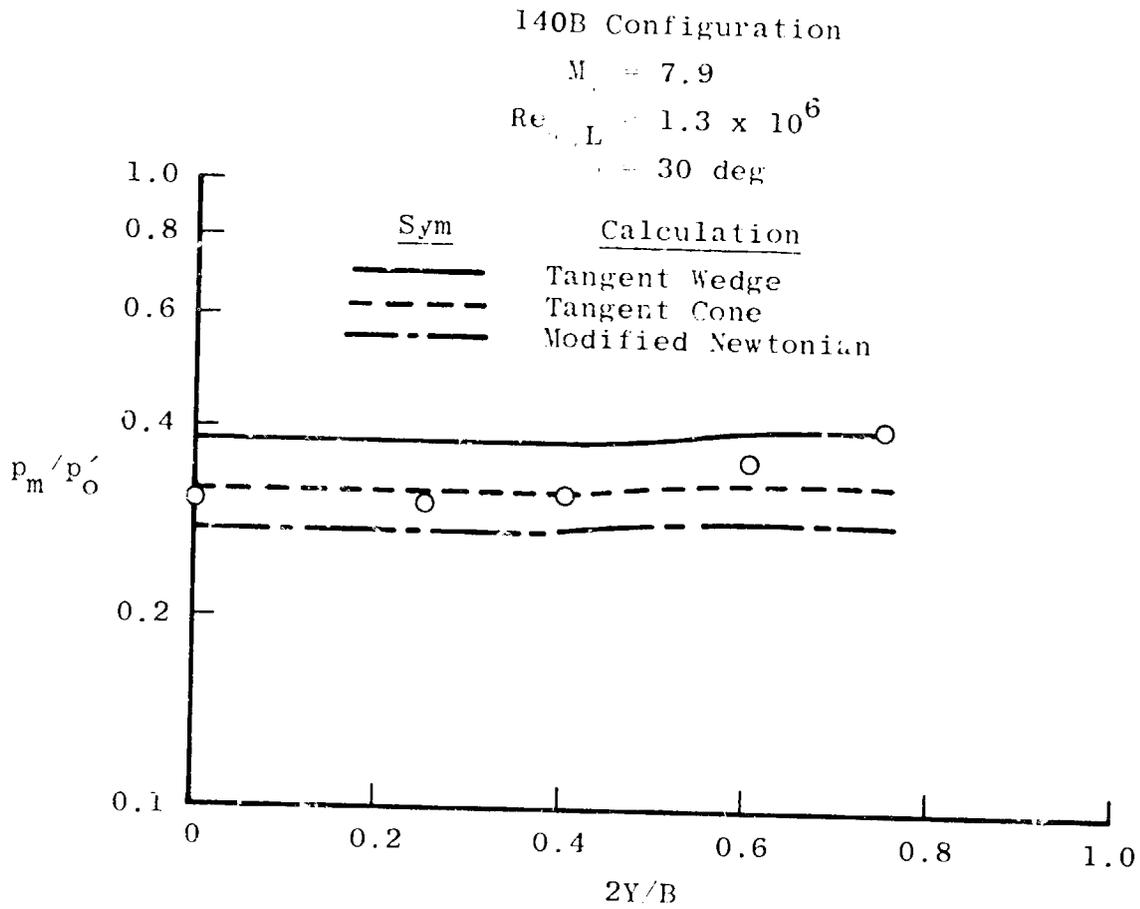
Figure 8. Spanwise surface static pressure distribution at
an X/L value of 0.8.
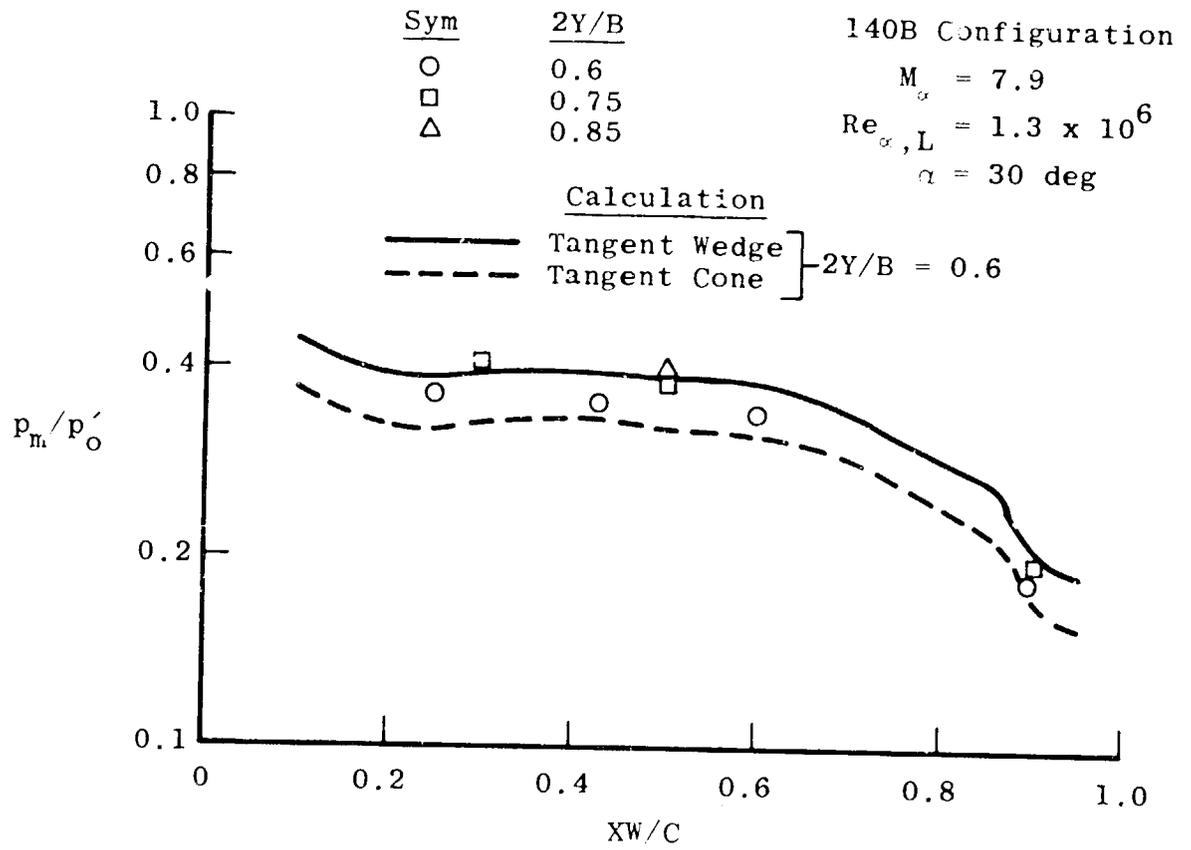
Figure 9. Wing surface static pressure distributions.
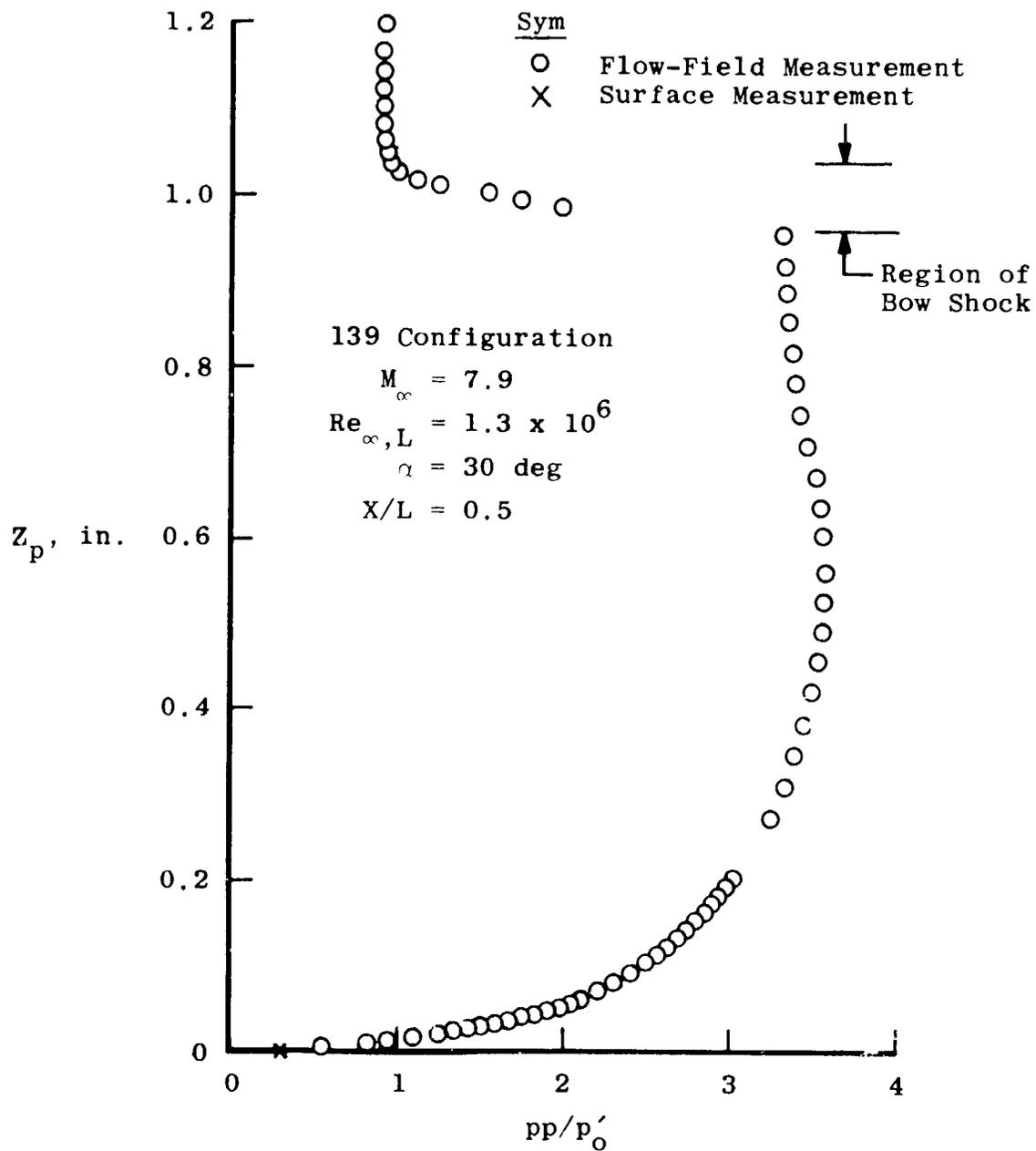
Figure 10. Typical centerline pitot pressure profile.
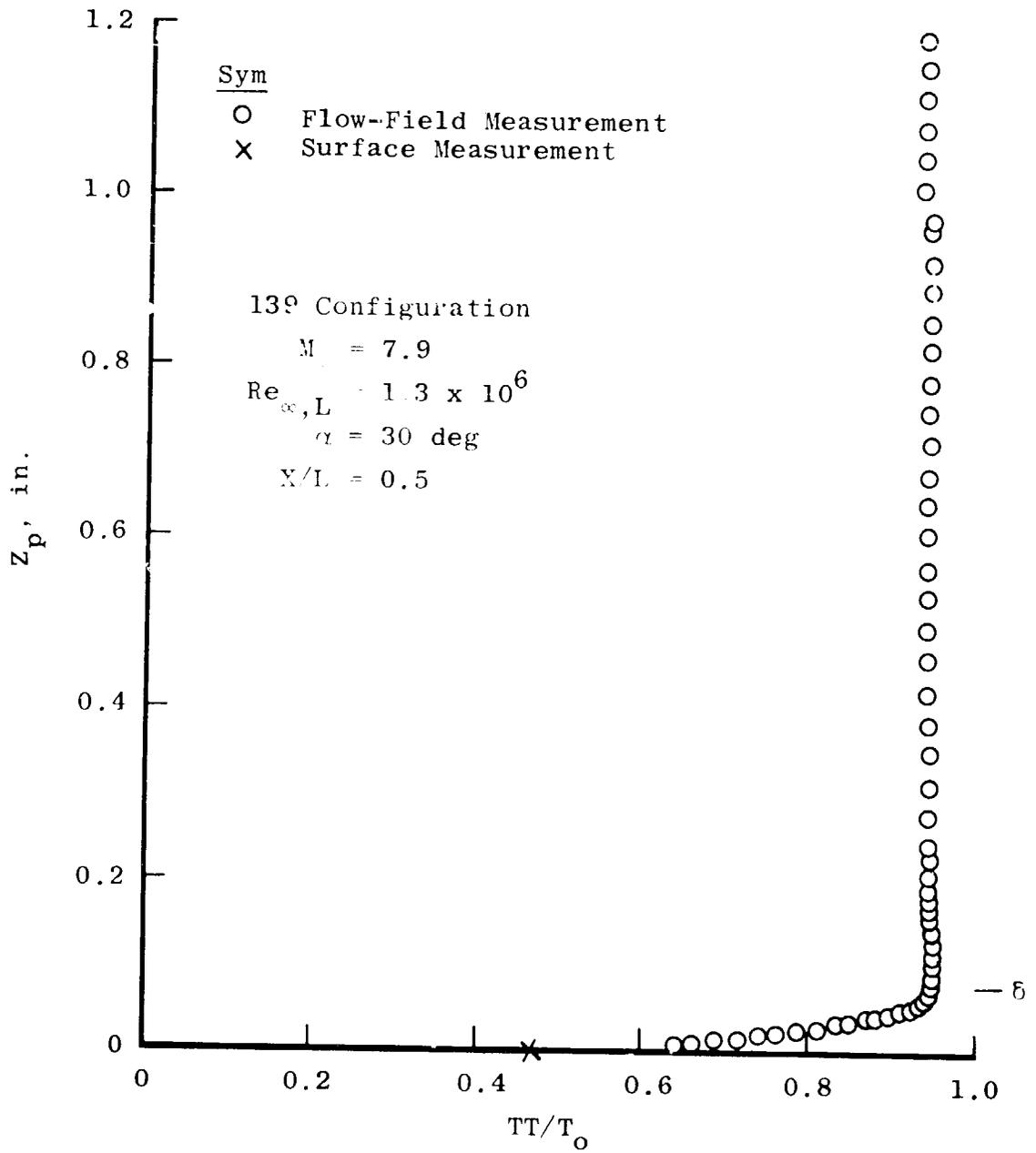
Figure 11. Typical centerline total-temperature distribution.
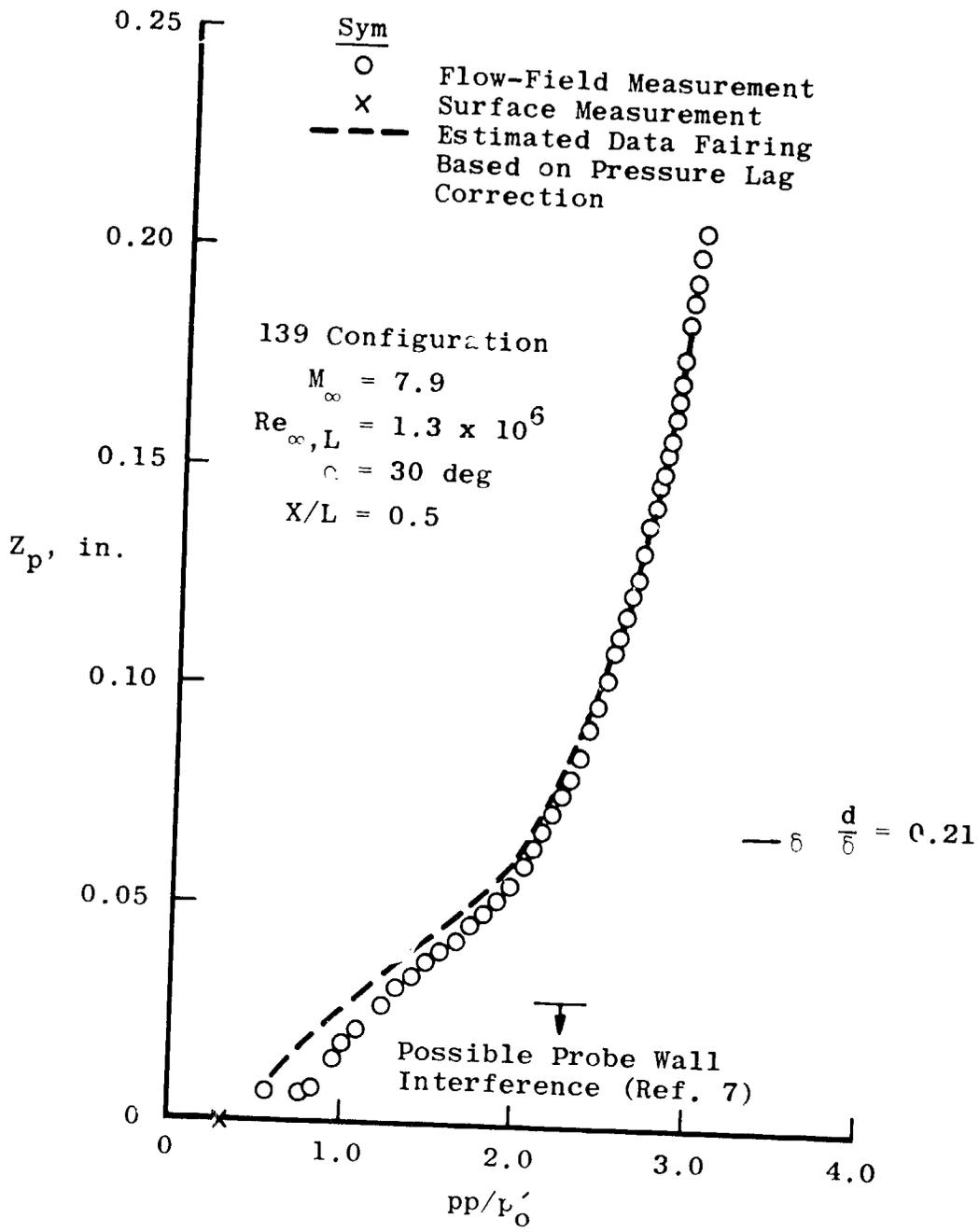
Figure 12. Detailed pitot pressure distribution.
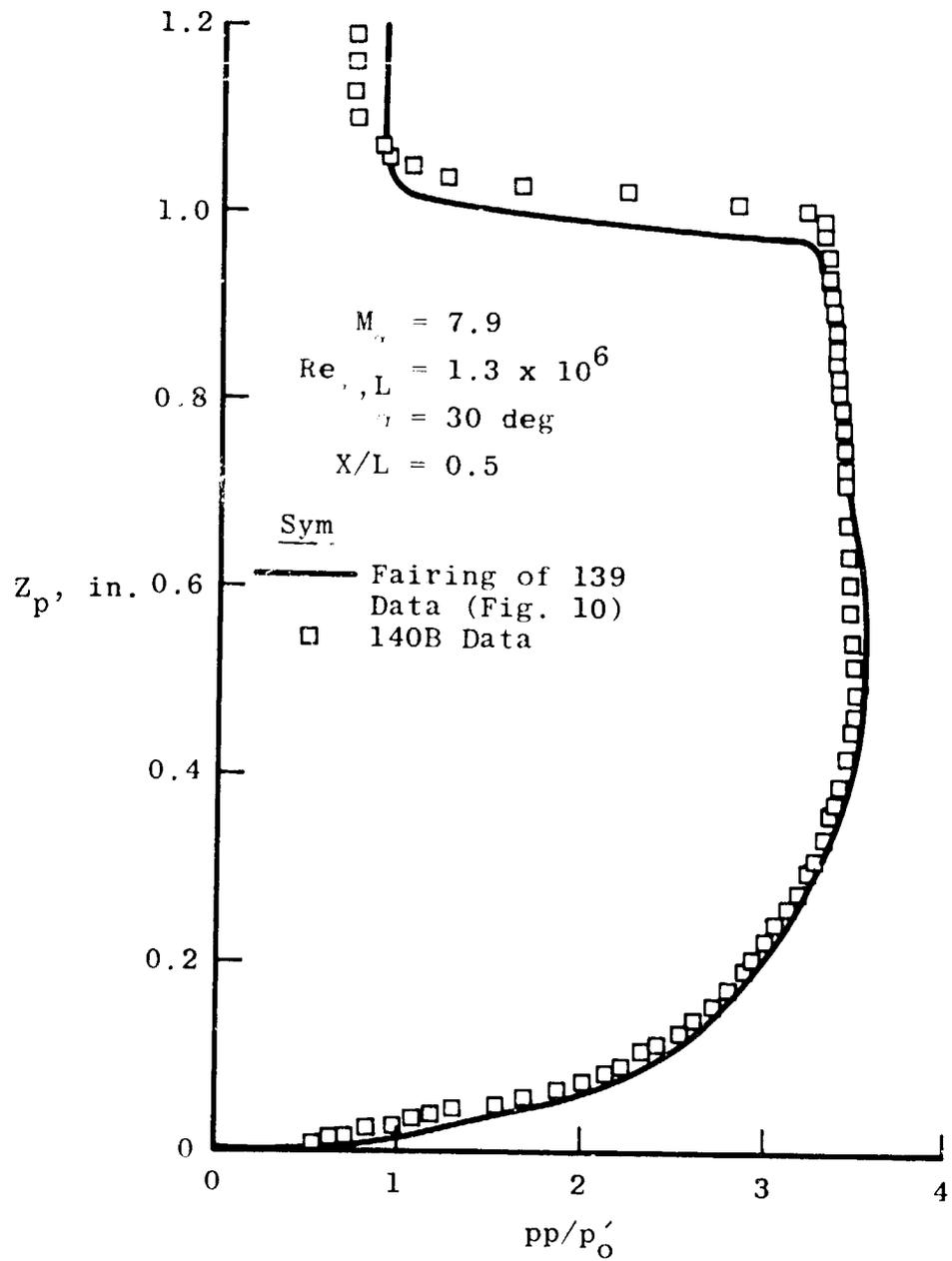
Figure 13. Comparison of 139 and 140B configurations pitot pressure profiles.
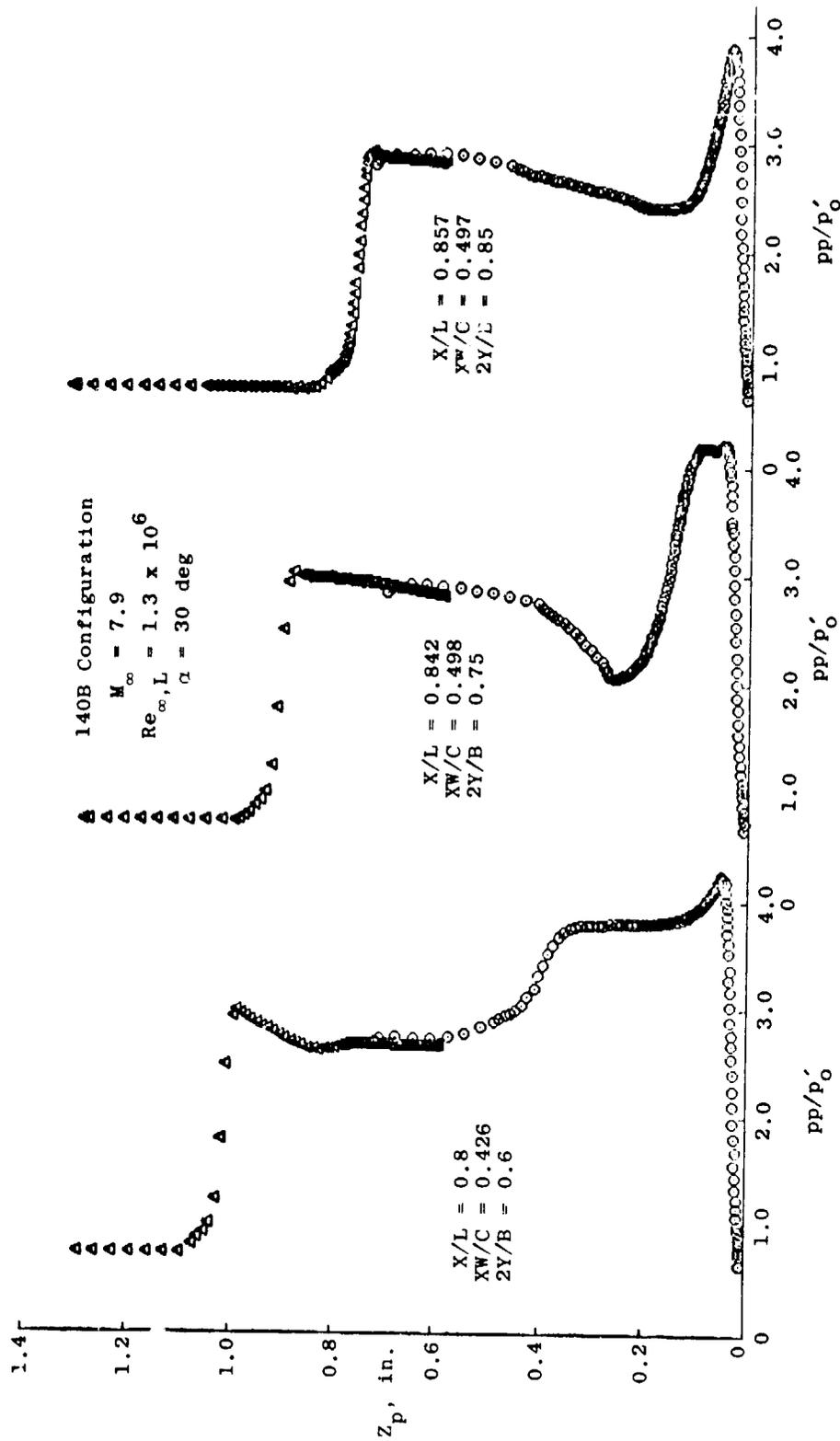
Figure 14. Wing pitot pressure profiles.

32
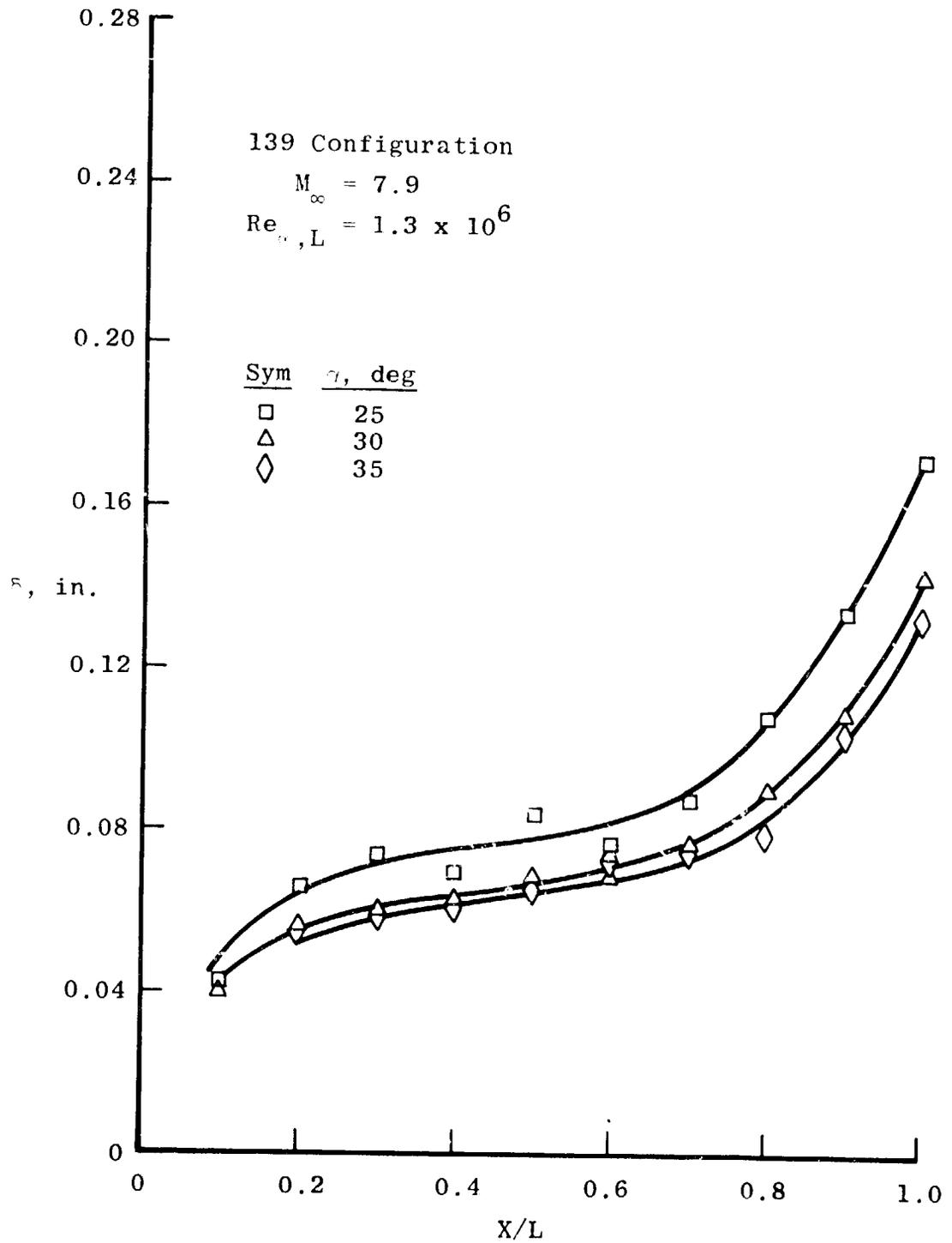
Figure 15. Centerline boundary-layer thickness distributions for the 139 configuration.

$$M_\infty = 7.9$$
$$Re_{\infty,L} = 1.3 \times 10^6$$
$$\alpha = 30 \text{ deg}$$

Sym

——————— 139 Data Fairing (Fig. 15)

□ 140B Data
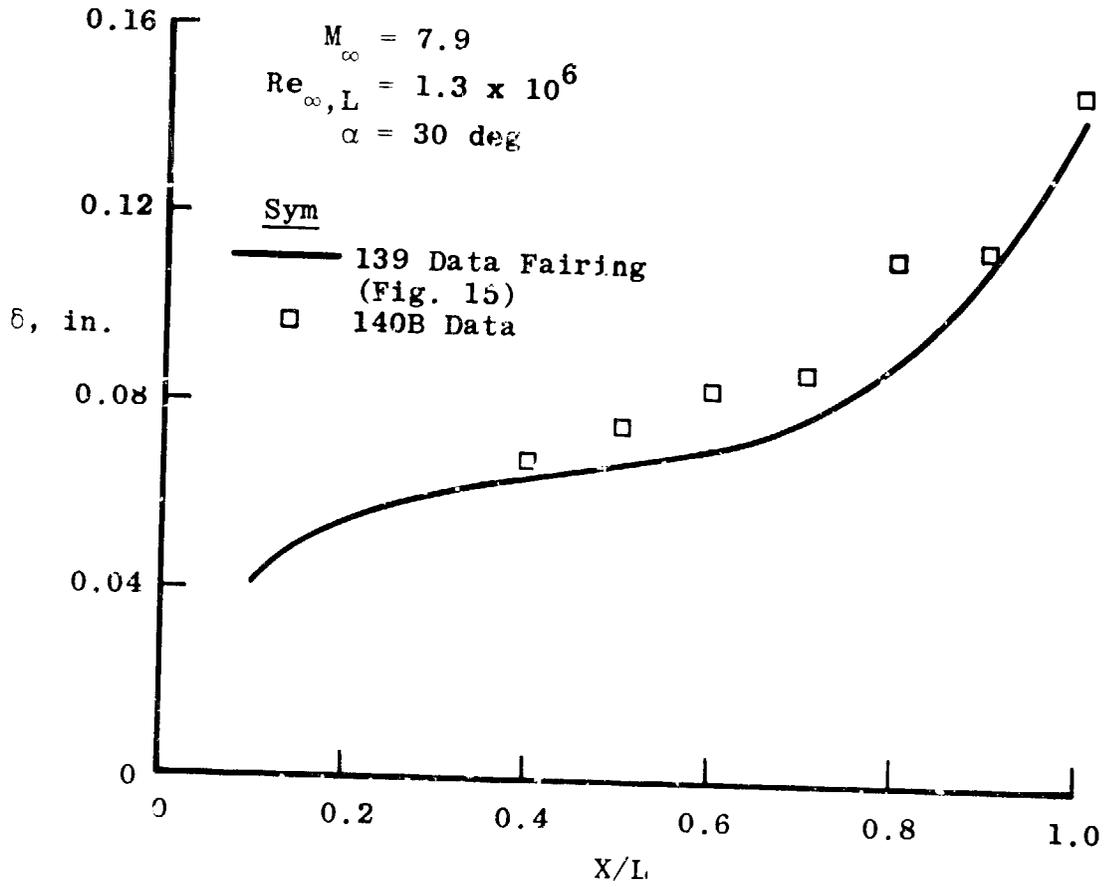
Figure 16. Comparison of boundary-layer thicknesses for 139 and 140B configurations.

140B Configuration

$M_\infty = 7.9$

$Re_{\infty,L} = 1.3 \times 10^6$

$\alpha = 30$ deg

$X/L = 0.8$

Data Fairing
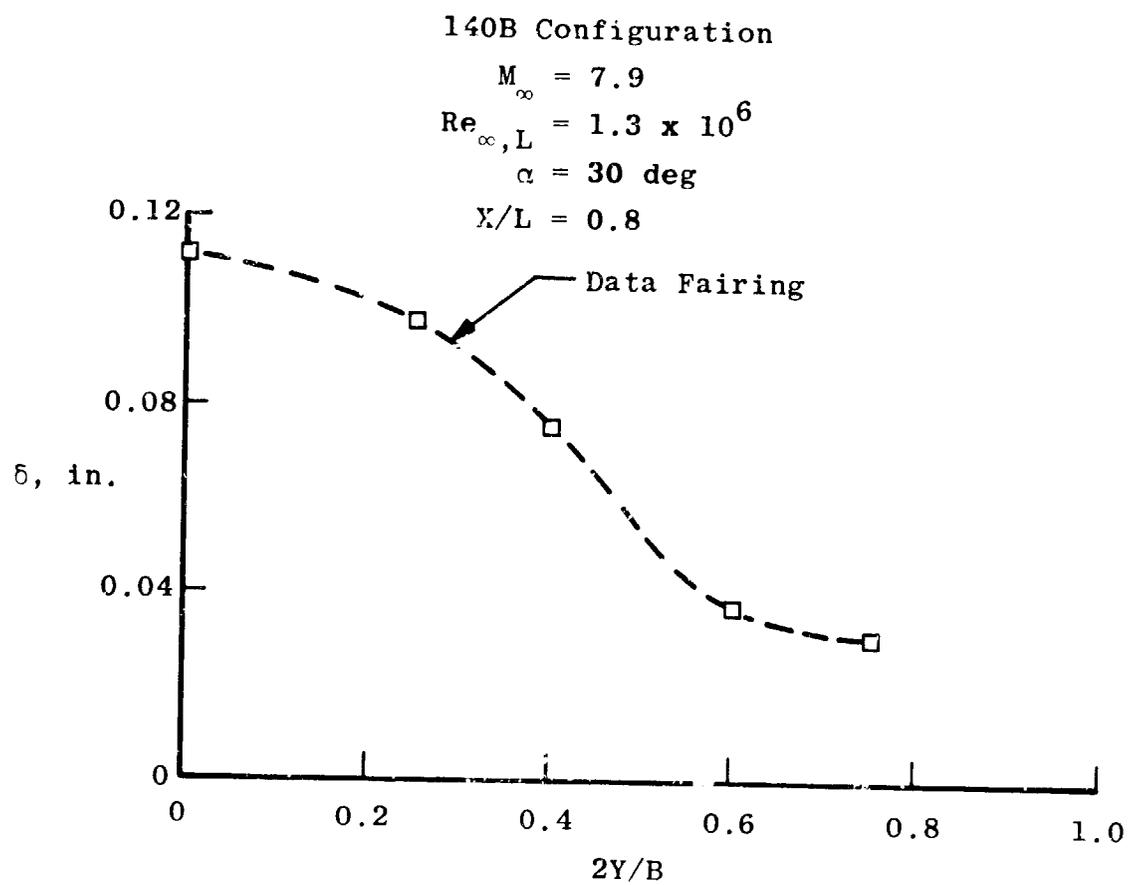
Figure 17. Spanwise boundary-layer thickness distribution at an X/L value of 0.8.
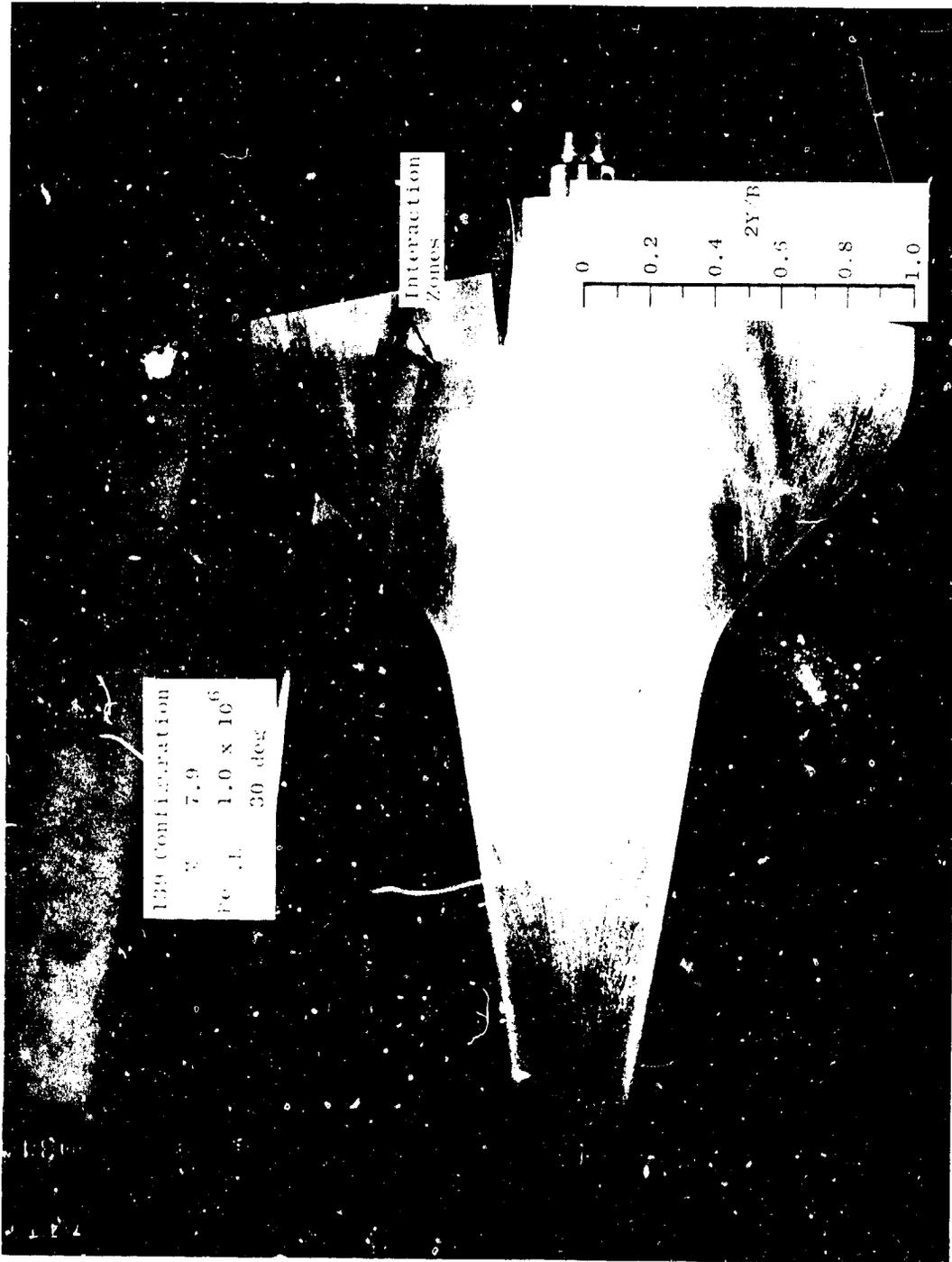
Figure 18. Oil flow photograph.
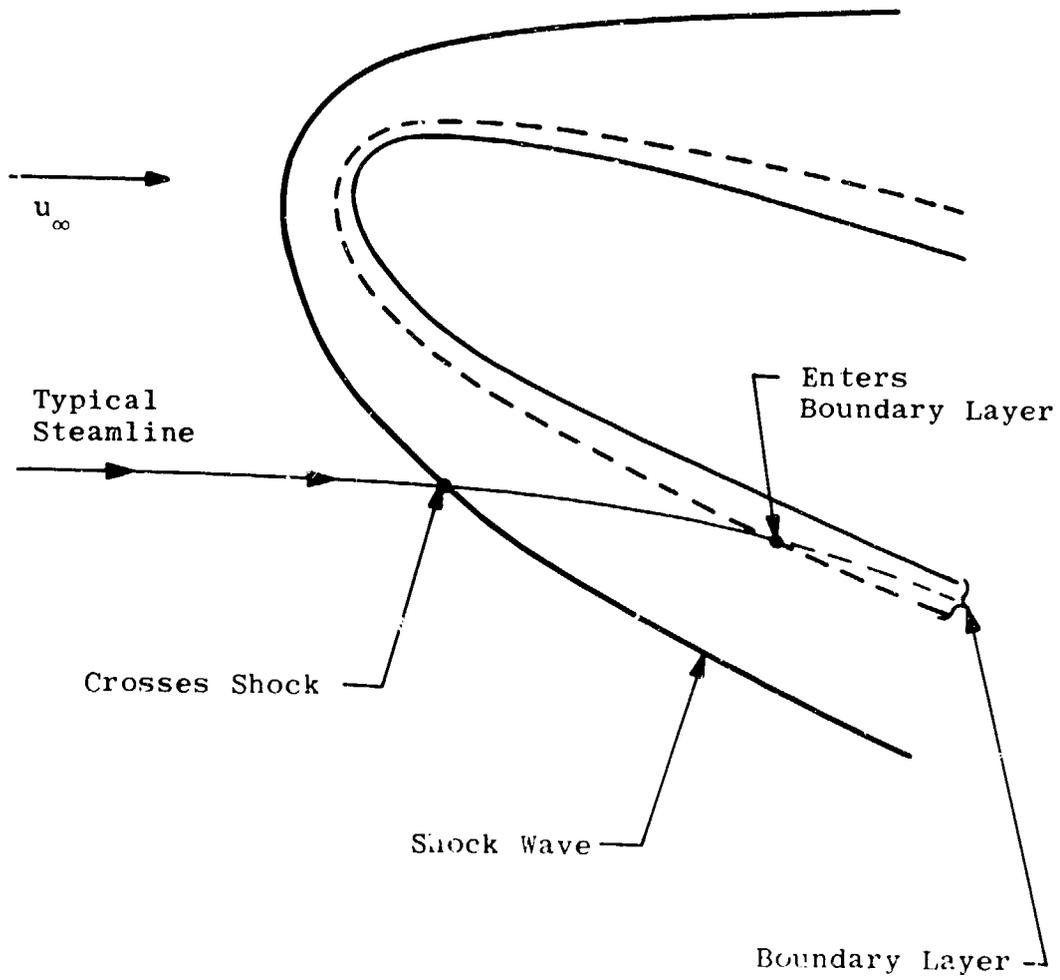
Figure 19. Flow-field illustration.
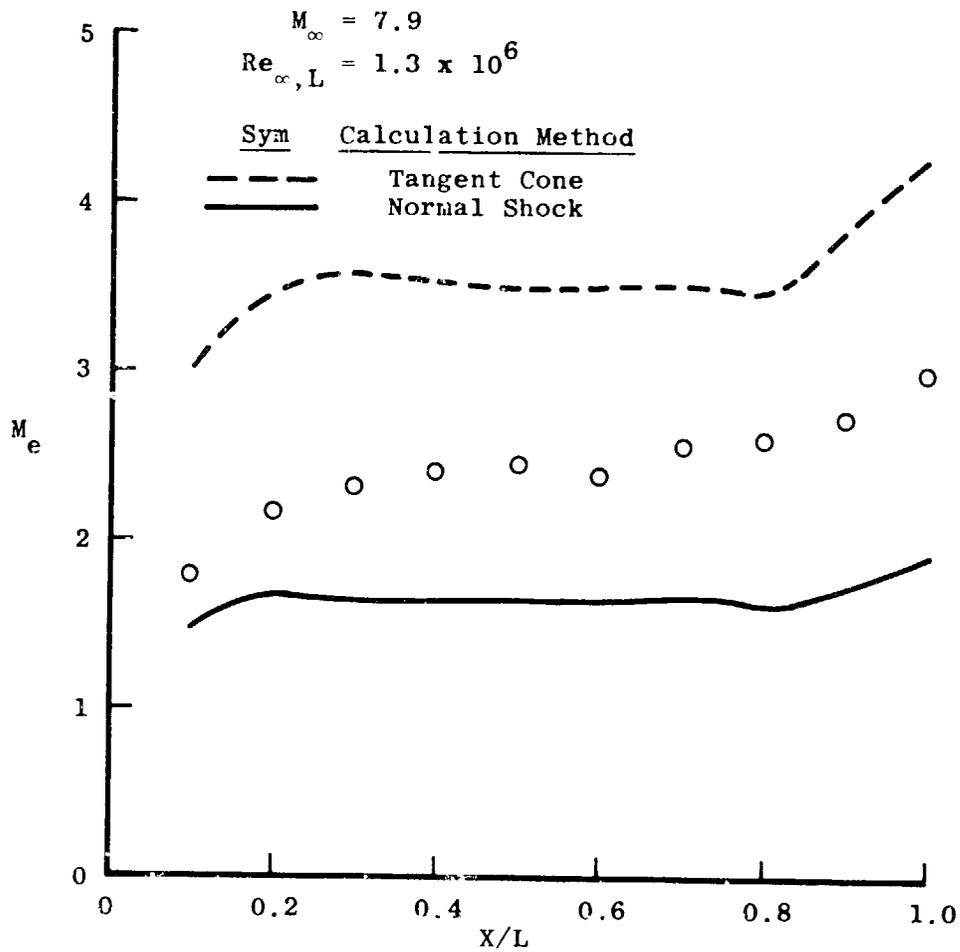
a. $\alpha = 25$ deg

Figure 20. Centerline boundary-layer-edge Mach number distributions for the 139 configuration.

$$M_\infty \quad 7.9$$

$$Re_{.L} \quad 1.2 \times 10^6$$

b. α = 30 deg
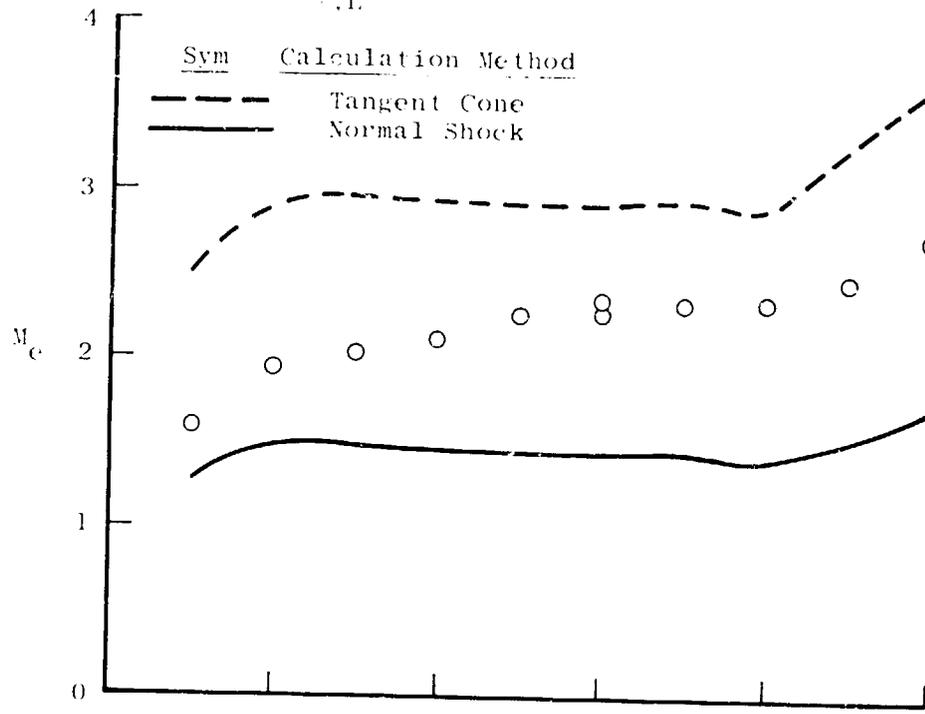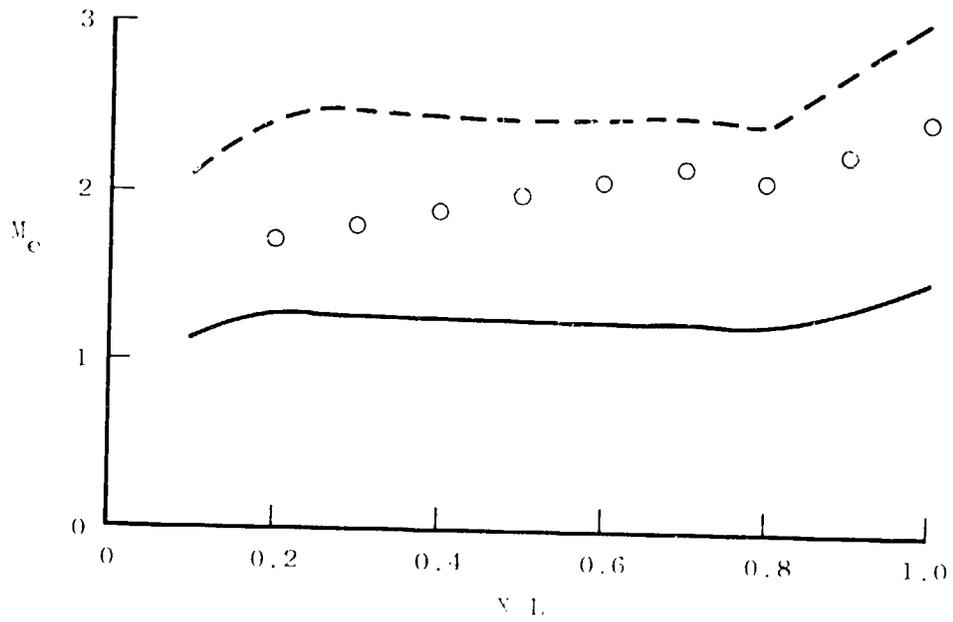
c. α = 35 deg

Figure 20. Concluded.

$$M_\infty = 7.9$$
$$Re_{\infty,L} = 1.3 \times 10^6$$
$$\alpha = 30 \ deg$$

——— Fairing of 139 Configuration Data (Fig. 20b)

□ 140B Configuration Data
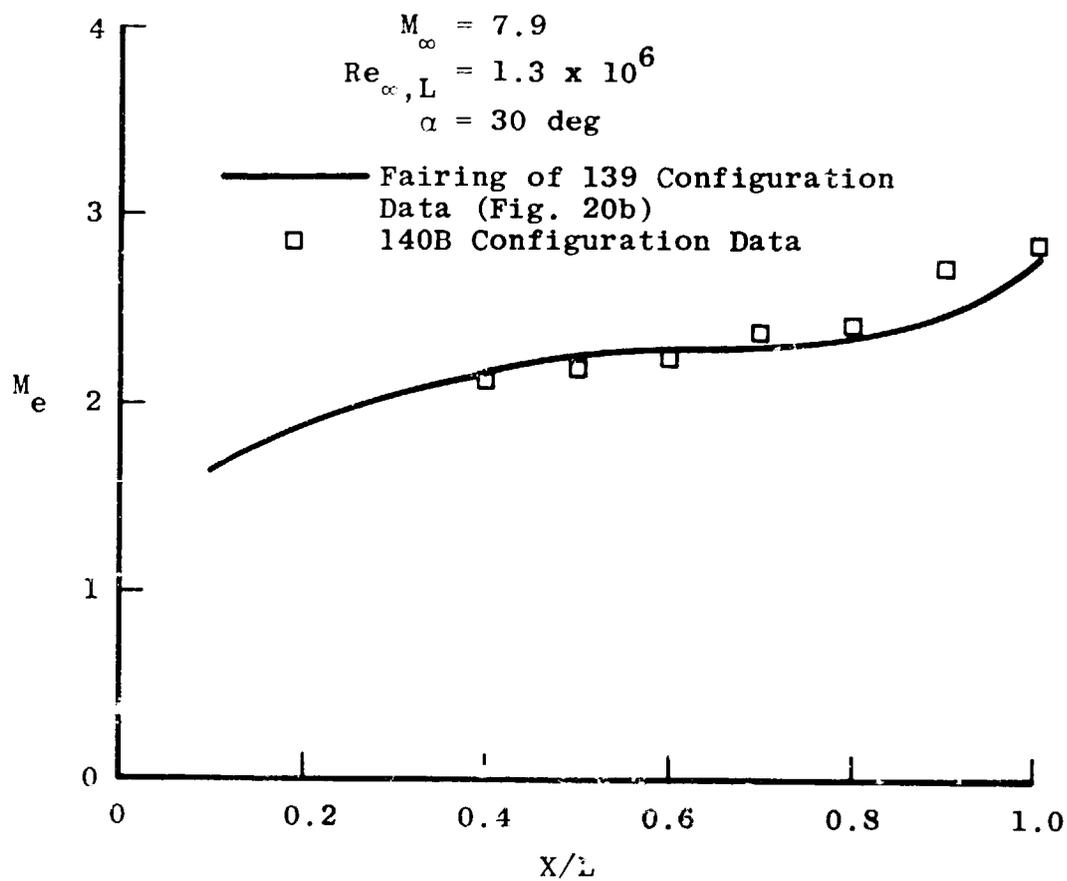
Figure 21. Comparison of 139 and 140B configuration centerline boundary-layer-edge Mach number distributions.

140B Configuration

$M_\alpha = 7.9$

$Re_{\alpha,L} = 1.3 \times 10^6$

$\alpha = 30$ deg

$X/L = 0.8$

Sym	Calculation Method
– – –	Tangent Cone
——	Tangent Wedge
—·—	Normal Shock
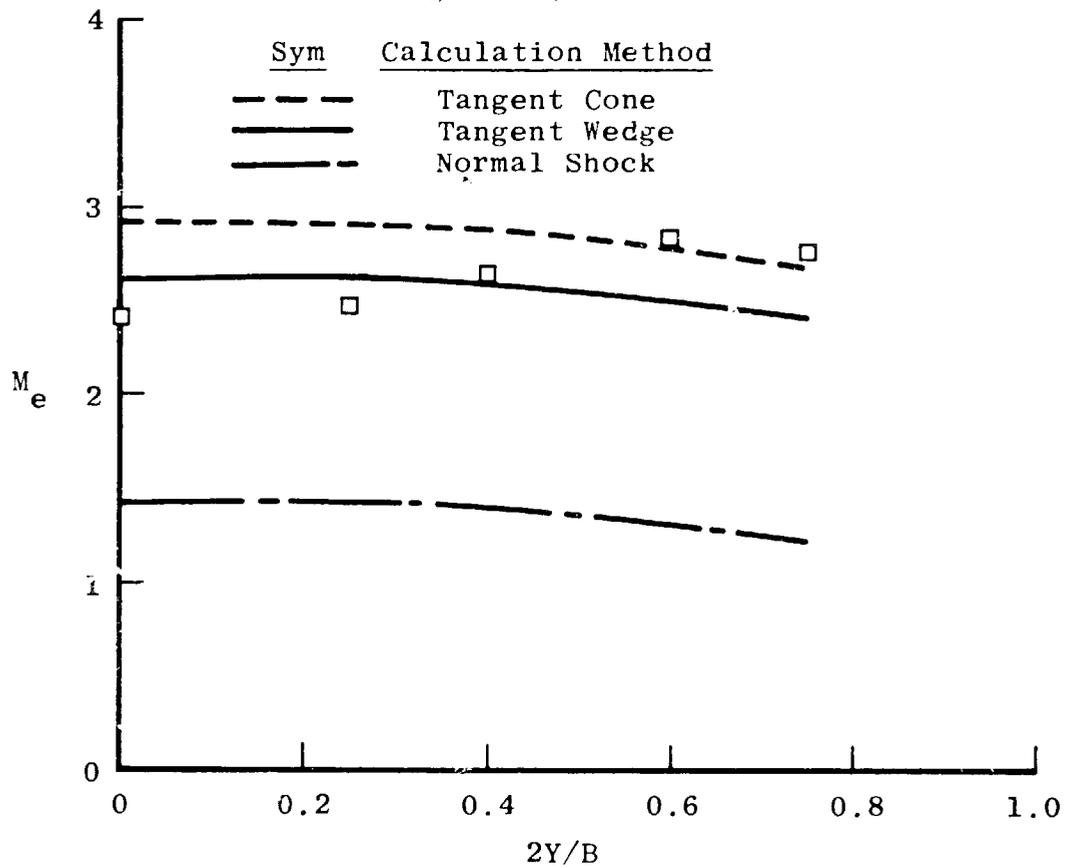
Figure 22. Spanwise boundary-layer-edge Mach number distribution at an X/L value of 0.8.

41
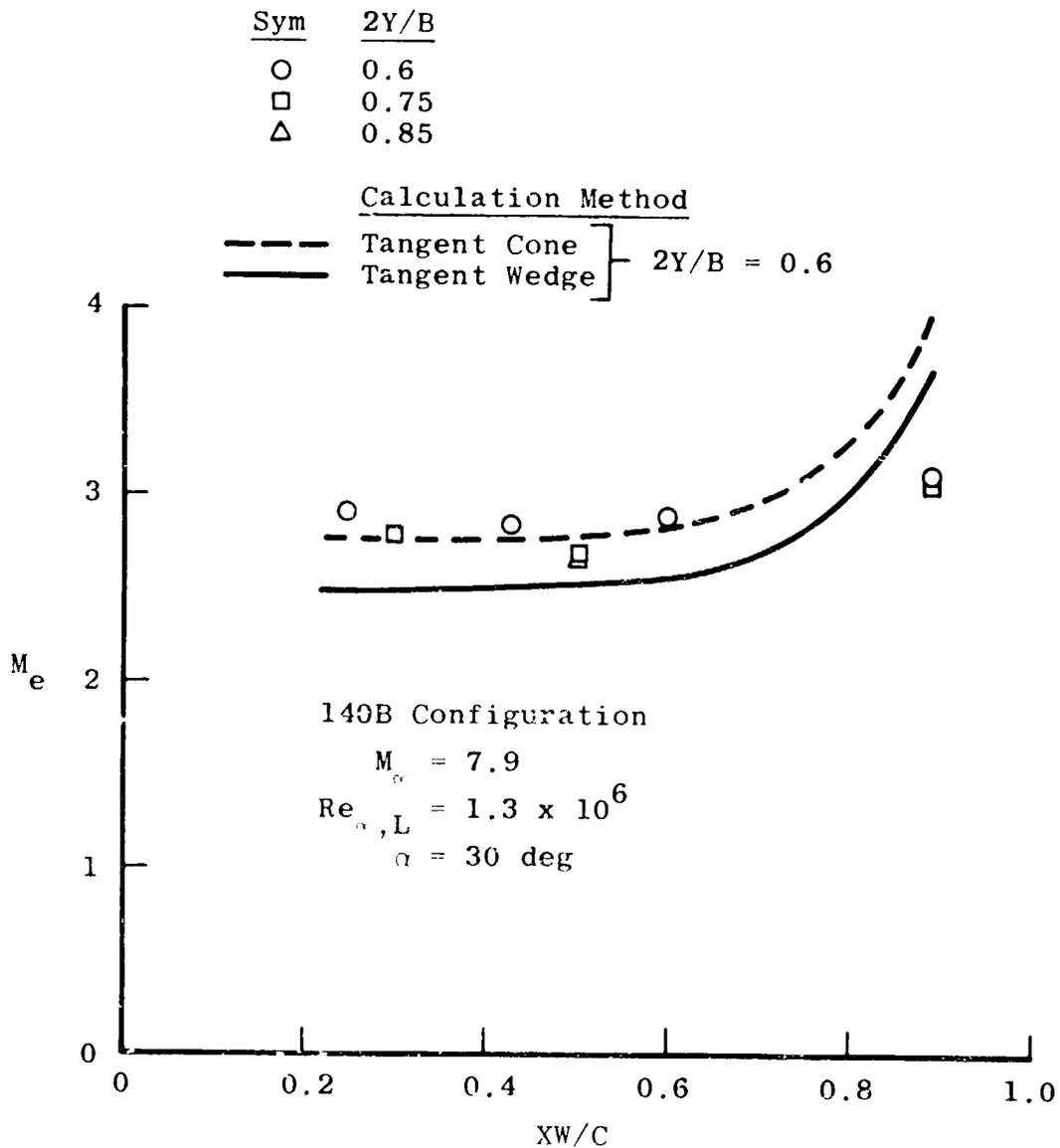
Figure 23. Wing boundary-layer-edge Mach number distributions.

Table 1. 139 Configuration Pressure Orifice and Thermocouple
Gage Locations

Pressure Orifice No.	X/L	2Y/B	XW/C	Pressure Orifice No.	X/L	2Y/B	XW/C
1	0.1	0	---	11	0.4	0.107	---
2	0.2		---	12	0.5	0.107	---
3	0.3		---	13	0.6	0.107	---
4	0.4		---	14	0.5	0.25	---
5	0.5		---	15	0.6	0.25	---
6	0.6		---	16	0.8	0.25	---
7	0.7		---	17	0.8	0.40	0.559
8	0.8		---	18	0.848	0.60	0.60
9	0.9		---	19	0.842	0.75	0.50
10	1.0		---	20	0.928	0.75	0.90
				21	0.857	0.85	0.50

Thermocouple No.	X/L	2Y/B
A	0.15	0
B	0.55	0
C	0.95	0

43

Table 2. 140B Configuration Pressure Orifice and Thermocouple
Gage Locations

Pressure Orifice No.	X/L	2Y/B	XW/C	Pressure Orifice No.	X/L	2Y/B	XW/C
1	0.1	0	---	14	0.5	0.25	---
2	0.2		---	15	0.6	0.25	---
3	0.3		---	16	0.8	0.25	---
4	0.4		---	17	0.8	0.4	0.556
5	0.5		---	18	0.847	0.6	0.599
6	0.6		---	19	0.842	0.75	0.498
7	0.7		---	20	0.928	0.75	0.900
8	0.8		---	21	0.857	0.85	0.497
9	0.9		---	22	0.7	0.25	---
10	1.0		---	23	0.750	0.6	0.246
11	0.4	0.107	---	24	0.8	0.6	0.426
12	0.5	0.107	---	25	0.928	0.6	0.889
13	0.6	0.107	---	26	0.8	0.75	0.299

Thermocouple No.	X/L	2Y/B	XW/C	Thermocouple No.	X/L	2Y/B	XW/C
A	0.15	0	---	F		0.40	0.777
B	0.55	0	---	G		0.60	0.734
C	0.95	0	---	H		0.85	0.662
D	0.88	0.75	0.699	I	0.55	0.25	---
E	0.88	0.25	---	J	0.70	0.40	0.299

Table 3. Test Summary

OH9 Test Phase (139 Configuration)

M_∞	p_O, psia	Survey Station Orifice No.	α, deg
7.92	150	1	15.5
		1	25
		1	30
		2-10	15.5
			25
			30
			35
		*	15.5
			25
			30
			35
7.95	250	2-10	30
7.95	250	*	30

OH5 Test Phase (140B Configuration)

M_∞	p_O, psia	Survey Station Orifice No.	α, deg
7.92	150	4-26	30
		21-26	35
		*	15
			25
			30
			35

*Surface pressure data (all orifices)

Table 4. Boundary-Layer-Edge Conditions - 139 Configuration

$Re_\infty/ft \times 10^{-6}$	α, deg	X/L	δ, in.	PP/P'_o	P_m/P'_o	P_m/PP	M_e	T_e/T_∞	a_e/a_∞	u_e/u_∞	ρ_e/ρ_∞	μ_e/μ_∞	Re_e/Re_∞
0.7	30.0	0.60	0.076	2.381	0.310	0.1302	2.355	6.422	2.5342	0.7535	3.921	5.440	0.5431
		0.40	0.063	1.830	0.295	0.1612	2.11	7.1652	2.6768	0.7131	3.344	5.960	0.4001
		0.30	0.060	1.658	0.290	0.1749	2.015	7.475	2.7341	0.6956	3.151	6.115	0.3584
		0.20	0.056	1.536	0.287	0.1868	1.94	7.728	2.7799	0.6809	3.016	6.241	0.3291
	25.0	0.10	0.040	1.421	0.375	0.2638	1.595	8.977	2.996	0.6034	3.393	6.950	0.2945
		0.60	0.076	2.333	0.310	0.1329	2.34	6.465	2.543	0.7512	3.895	5.493	0.5326
		0.50	0.084	1.848	0.225	0.12175	2.45	6.155	2.481	0.7675	2.969	5.298	0.4301
		0.40	0.069	1.704	0.215	0.1262	2.405	6.280	2.506	0.7610	2.781	5.385	0.3930
		0.30	0.074	1.511	0.205	0.1357	2.31	6.552	2.560	0.7466	2.541	5.568	0.3407
		0.20	0.066	1.405	0.215	0.1530	2.17	6.975	2.641	0.7236	2.503	5.835	0.3104
	15.5	0.10	0.042	1.314	0.285	0.2169	1.79	8.255	2.873	0.6494	2.804	6.581	0.2767
		0.30	0.104	0.887	0.0825	0.0930	2.825	5.217	2.284	0.8148	1.284	4.684	0.2234
	35.0	0.20	0.092	0.922	0.120	0.1301	2.37	6.379	2.526	0.7558	1.528	5.451	0.2119
		0.10	0.056	1.010	0.150	0.1485	2.20	6.883	2.624	0.7288	1.770	5.758	0.2240
		0.70	0.076	2.521	0.388	0.1539	2.16	7.007	2.647	0.7219	4.498	5.833	0.5567
		0.60	0.074	2.388	0.399	0.1671	2.07	7.294	2.701	0.7059	4.443	6.006	0.5222
		0.50	0.066	2.188	0.390	0.1782	1.99	7.559	2.749	0.5908	4.191	6.160	0.4699
		0.40	0.061	1.965	0.385	0.1959	1.89	7.901	2.811	0.6708	3.958	6.359	0.4174
	30.0	0.30	0.058	1.749	0.79	0.2167	1.79	8.255	2.873	0.6493	3.729	6.558	0.3692
		0.20	0.055	1.570	0.373	0.2345	1.71	8.547	2.923	0.6312	3.545	6.720	0.3329
		0.50	0.068	2.148	0.305	0.1420	2.26	6.701	2.588	0.7386	3.697	5.648	0.4835
		0.40	0.061	1.775	0.295	0.1662	2.07	7.345	2.710	0.7057	3.287	6.033	0.3845
1.1		0.50	0.055	2.008	0.305	0.1519	2.18	6.993	2.645	0.7251	3.969	5.836	0.4435
		0.30	0.043	1.613	0.293	0.1816	1.97	7.680	2.771	0.6867	3.122	6.256	0.3427

Table 4. Concluded

$Re_\infty/ft \times 10^{-6}$	α, deg	X/L	δ, in.	PP/P'$_o$	P$_m$/P'$_o$	P$_m$/PP	M$_e$	T$_e$/$_\cdot$	a$_e$/a$_\infty$	u$_e$/u$_\infty$	ρ_e/ρ_∞	μ_e/μ_∞	Re$_e$/Re$_\infty$
0.7	30.0	0.60	0.069	2.187	0.310	0.1417	2.26	6.701	.588	0.7386	3.7579	5.661	0.4904
		1.00	0.143	2.041	0.205	0.1004	2.71	5.487	2.342	0.8015	3.0349	4.872	0.4993
		0.90	0.109	2.221	0.270	0.1216	2.45	6.155	2.481	0.7675	3.5628	5.213	0.5146
		0.80	0.091	2.383	0.319	0.1339	2.33	6.494	2.548	0.7497	3.9899	5.527	0.5412
		0.70	0.077	2.197	0.300	0.1365	2.305	6.567	2.563	0.7458	3.7106	5.572	0.4967
	35.0	1.00	0.132	2.285	0.280	0.1225	2.44	6.183	2.486	0.7661	3.6782	5.326	0.5291
		0.90	0.104	2.432	0.350	0.1439	2.24	6.761	2.600	0.7354	4.2050	5.687	0.5438
		0.80	0.079	2.461	0.405	0.1646	2.08	7.262	2.695	0.7077	4.5301	5.990	0.5352
	25.0	1.00	0.172	1.797	0.150	0.0835	2.99	4.858	2.204	0.8321	2.5078	4.425	0.4716
		0.90	0.134	2.017	0.200	0.0992	2.73	5.439	2.332	0.8039	2.9870	4.836	0.4966
		0.80	0.108	2.199	0.237	0.1078	2.61	5.734	2.375	0.7891	3.3574	5.036	0.5260
		0.70	0.088	1.933	0.217	0.1123	2.56	5.862	2.421	0.7826	3.0068	5.124	0.4592
		0.60	0.077	1.758	0.227	0.1291	2.37	6.379	2.526	0.7558	2.8904	5.459	0.4002
	15.5	1.00	0.283	1.023	0.107	0.1046	2.66	5.608	2.368	0.7954	1.5496	4.950	0.249
		0.90	0.222	1.210	0.106	0.0883	2.90	5.050	2.247	0.8229	1.7048	4.561	0.308
		0.80	0.181	1.358	0.103	0.0758	3.14	4.558	2.135	0.8464	1.8356	4.202	0.369
		0.70	0.143	1.206	0.096	0.0796	3.06	4.715	2.171	0.8389	1.6537	4.315	0.322
		0.60	0.141	1.114	0.0915	0.0821	3.01	4.817	2.195	0.8341	1.5329	4.389	0.293
		0.50	0.124	1.009	0.088	0.0872	2.92	5.007	2.338	0.825	1.4276	4.528	0.260
		0.40	0.102	1.229	Bad								
1.1	30.0	0.30	0.104	0.820	0.0825	0.1006	2.71	5.486	2.342	0.8015	1.2214	4.869	0.201
		0.20	0.085	0.864	0.120	0.1389	2.29	6.611	2.571	0.7434	1.4743	5.608	0.1954
		0.60	0.065	2.115	0.320	0.1513	2.18	6.993	2.644	0.7251	3.745	5.848	0.4643
		1.00	0.131	2.021	0.205	0.1014	2.70	5.549	2.356	0.8000	3.023	4.913	0.4922
		0.80	0.077	2.390	0.319	0.1335	2.33	6.540	2.557	0.7495	3.992	5.557	0.5384
		0.70	0.070	2.226	0.303	0.1361	2.31	6.598	2.569	0.7464	3.758	5.600	0.5009
		0.90	0.103	2.153	0.265	0.1231	2.435	6.240	2.498	0.7651	3.475	5.385	0.4938

Table 5. Boundary-Layer-Edge Conditions - 140B Configuration

$Re_\infty/ft \times 10^{-6}$	α, deg	X/L	Y, in.	δ, in.	pp/p'_o	p_m/p'_o	p_m/pp	M_e	T_e/T_∞	a_e/a_∞	u_e/u_∞	ρ_e/ρ_∞	μ_e/μ_∞	Re_e/Re_∞
0.7	30	0.4	0	0.068	1.899	0.3042	0.1602	2.115	7.1492	2.6738	0.71403	3.456	5.91	0.41756
		0.5	0	0.076	2.038	0.3075	0.1509	2.185	6.9291	2.632	0.7262	3.605	5.77	0.4534
		0.6	0	0.083	2.213	0.3160	0.1428	2.25	6.73	2.594	0.737	3.813	5.657	0.4968
		0.7	0	0.097	2.464	0.3156	0.1281	2.385	6.3365	2.517	0.758	4.0455	5.4165	0.5662
		0.8	0	0.112	2.441	0.3059	0.1253	2.41	6.266	2.503	0.7617	3.965	5.366	0.563
		0.9	0	0.114	2.150	0.2155	0.1002	2.715	5.4745	2.339	0.802	3.197	4.8465	0.529
		1.0	0	0.148	1.915	0.1743	0.0910	2.86	5.1387	2.267	0.8186	2.755	4.6130	0.4889
		0.4	0.88	0.059	1.830	0.3041	0.1662	2.07	7.294	2.701	0.7059	3.386	5.9905	0.399
		0.5		0.072	1.847	0.3100	0.1678	2.06	7.3268	2.7068	0.7040	3.4367	6.0096	0.4026
		0.6		0.067	2.133	0.3167	0.1485	2.20	6.883	2.6235	0.7287	3.7375	5.747	0.474
		0.5	2.05	0.064	2.25	0.3176	0.1427	2.25	6.7306	2.594	0.737	3.833	5.6574	0.4993
		0.6		0.075	2.415	0.3438	0.1424	2.25	6.7306	2.594	0.737	4.149	5.6574	0.5405
		0.7		0.107	2.50	0.3068	0.1227	2.44	6.183	2.4866	0.7661	4.0304	5.316	0.5808
		0.8	3.28	0.098	2.542	0.3000	0.1180	2.49	6.0469	2.459	0.7661	4.0297	5.2285	0.5959
		0.8	4.92	0.076	2.920	0.3071	0.1052	2.65	5.6333	2.3735	0.7731	.428	4.956	0.7095
		0.75		0.030	4.264	0.3691	0.08656	2.93	4.9854	2.2328	0.794	6.0136	4.5088	1.1017
	35	0.8	6.15	0.037	3.949	0.3597	0.0911	2.85	5.1611	2.2718	0.8175	5.661	4.6306	0.9994
		0.85		0.044	3.757	0.3343	0.08898	2.89	5.0723	2.2522	0.8218	5.3533	4.5684	0.963
		0.93		0.058	2.35	0.1817	0.7732	3.11	4.616	2.1485	0.8437	3.1973	4.2405	0.6361
		0.8	6.97	0.031	4.185	0.404	0.09653	2.77	5.3442	2.3117	0.8085	6.14	4.7608	1.0428
		0.84		0.036	3.72	0.3781	0.10164	2.70	5.5107	2.3475	0.8003	5.5731	4.8757	0.9147
		0.93		0.058	2.465	0.1971	0.07996	3.06	4.7151	2.1714	0.839	3.3953	4.3176	0.6598
		0.86	6.97	0.036	3.841	0.3960	0.1031	2.68	5.5594	2.3576	0.7978	5.7858	4.9121	0.9397
		0.86		0.032	3.97	0.4791	0.12068	2.46	6.1282	2.4755	0.7689	6.3502	5.2876	0.9234
		0.93	6.15	0.053	2.617	0.2490	0.09515	2.79	5.2977	2.3017	0.8108	3.7564	4.733	0.6435
		0.84		0.036	3.628	0.4635	0.12776	2.39	6.3224	2.5144	0.7588	5.9547	5.4104	0.8351
		0.80		0.031	3.936	0.4981	0.12655	2.40	6.2943	2.5088	0.7603	6.4278	5.3879	0.9067
		0.93	4.92	0.059	2.487	0.2299	0.09244	2.83	5.206	2.2817	0.8153	3.5869	4.6631	0.6271

APPENDIX A
DATA REDUCTION EQUATIONS

The following equations were used to compute the boundary-layer-edge conditions which are given in Tables 4 and 5.

PARAMETER	EQUATION

pp/p_m

$$pp/p_m = \frac{pp/p_o'}{p_m/p_o'}$$

M_e

From Table II, Ref. 8 using pp/p_m

T_e/T_∞

$$T_e/T_\infty = \left[1 + \frac{(\gamma - 1)\, M_\infty^2}{2}\right] \Big/ \left[1 + \frac{(\gamma - 1)\, M_e^2}{2}\right]$$

a_e/a_∞

$$a_e/a_\infty = (T_e/T_\infty)^{1/2}$$

u_e/u_∞

$$u_e/u_\infty = (M_e/M_\infty)(a_e/a_\infty)$$

ρ_e/ρ_∞

$$\rho_e/\rho_\infty \left[\frac{p_m}{p_o'}\right] \left[\frac{(\gamma+1)\, M_\infty^2}{2}\right]^{\frac{\gamma}{\gamma-1}} \left[\frac{\gamma+1}{2\gamma M_\infty^2 - (\gamma-1)}\right]^{\frac{1}{\gamma-1}} \Big/ \left(\frac{T_e}{T_\infty}\right)$$

μ_e/μ_∞

$$\mu = \frac{2.27 \times 10^{-8}\, T^{3/2}}{T + 198.6}, \quad \frac{\text{lb sec}}{\text{ft}^2} \quad (\text{for } T > 200°R)$$

$$\mu = 8.051 \times 10^{-10}\, T, \quad \frac{\text{lb sec}}{\text{ft}^2} \quad (\text{for } T < 200°R)$$

Re_e/Re_∞

$$Re_e/Re_\infty = (\rho_e/\rho_\infty)(u_e/u_\infty)\,/\,(\mu_e/\mu_\infty)$$

49

NOMENCLATURE

a	Speed of sound, ft/sec
B	Model total span, 16.40 in.
C	Local wing chord
C_p	Pressure coefficient, $(p_m - p_\infty)/q_\infty$
d	Probe tip diameter, in.
L	Model reference length, 22.58 in. (139) or 22.63 in. (140B)
M	Mach number
p	Static pressure, psia
p_m	Model surface static pressure, psia
p_o	Tunnel stilling chamber pressure, psia
p_o'	Free-stream pitot pressure, psia
pp	Survey pitot pressure, psia
q_∞	Free-stream dynamic pressure, psia
Re	Reynolds number
Re/ft	Unit Reynolds number, ft^{-1}
T	Static temperature, °R
T_o	Tunnel stilling chamber temperature, °R
TT	Survey total temperature, °R
u	Velocity, ft/sec
X	Axial distance from the nose, in.

XW   Axial distance from the wing leading edge, in.

Y   Lateral distance from the model centerline, in.

Z_p Probe height above model surface along the survey probe
            drive axis, in.

α Model angle of attack, deg

δ Boundary-layer thickness, in.

ϵ Local body deflection angle with respect to the X-Y plane, deg

γ Ratio of specific heats (1.40 for air)

μ Viscosity, lb-sec/ft^2

ρ Density, slug/ft^3

SUBSCRIPTS

e   Boundary-layer-edge condition

L   Based on model reference length

max   Maximum value

∞ Free-stream condition

1   Probe 1

2   Probe 2